

Technical Report

**TR-19-12**

April 2019



# Assessment of microstructural changes in copper due to gamma radiation damage

Cristiano Padovani  
Dimitri Pletser  
Kerstin Jurkschat  
David Armstrong  
Stephen Dugdale  
Daniel Brunt  
Roy Faulkner  
Gary Was  
Adam Johannes Johansson

SVENSK KÄRNBRÄNSLEHANTERING AB

SWEDISH NUCLEAR FUEL  
AND WASTE MANAGEMENT CO

Box 3091, SE-169 03 Solna  
Phone +46 8 459 84 00  
skb.se

SVENSK KÄRNBRÄNSLEHANTERING



ISSN 1404-0344

**SKB TR-19-12**

ID 1708197

April 2019

# **Assessment of microstructural changes in copper due to gamma radiation damage**

Cristiano Padovani, Dimitri Pletser  
Wood

Kerstin Jurkschat, David Armstrong  
University of Oxford

Stephen Dugdale  
University of Bristol

Daniel Brunt  
National Physical Laboratory

Roy Faulkner  
Loughborough Materials

Gary Was  
University of Michigan

Adam Johannes Johansson  
Svensk Kärnbränslehantering AB

A pdf version of this document can be downloaded from [www.skb.se](http://www.skb.se).

© 2019 Svensk Kärnbränslehantering AB

---

<b>Figure no</b>	<b>Credits</b>
------------------	----------------

---

4-1	Reprinted from Modern Problems in Condensed Matter Sciences, P. Ehrhart, K. H. Robrock, H. R. Schober, Basic Defects in Metals, Chapter 1, Copyright (1986), with permission from Elsevier
-----	--

---

# Executive summary

An experimental programme was designed and implemented to carry out a pre-study examining the effects of gamma radiation on the concentration of crystalline and microstructural defects in copper at doses relevant to the spent nuclear fuel disposal concept KBS-3. The work was carried out attempting to experimentally underpin previous computational findings. According to such studies, neglecting thermal annealing processes,  $\gamma$  radiation may be able to induce point defects in concentrations of  $10^{-10}$ – $10^{-9}$  dpa in copper samples subjected to the total  $\gamma$  dose of circa 100 kGy expected in a repository. In light of the small concentrations, the experimental work presented in this report made use of very sensitive imaging and microstructural characterisation techniques to attempt to detect any defects induced by  $\gamma$  radiation. Theoretical work was also carried out after completion of the measurements to evaluate the concentration of defects in the material in relevant conditions and compare it with the expected sensitivity of different techniques and their ability to probe a sufficiently high volume of material to yield confidence in the observations. A quantitative theoretical examination of the effects of thermal annealing and the role it may play in the detection of radiation-induced defects in relevant conditions was also carried out.

Copper samples were irradiated, under an inert atmosphere, up to a full repository dose of 100 kGy. Dose rates were approximately 1 kGy/hour, ensuring that the full dose was reached within less than a week of irradiation. Post-irradiation examination was performed on irradiated samples using High-Resolution Transmission Electron Microscopy (HR-TEM), nanoindentation, Positron Annihilation Lifetime Spectroscopy (PALS) and electrical resistivity measurements. Data from these measurements was compared against measurements done on unirradiated control samples to estimate the effect gamma irradiation had on defect density, material microstructure and selected material properties. Gamma radiation was found to have no effects on the copper's properties and microstructure within the sensitivity and "representativeness" (i.e. ability to probe volumes that produce statistically significant results) of the techniques employed. In particular:

- HR-TEM showed no detectable difference between irradiated and unirradiated samples. However, it also indicated a high concentration of dislocations, dislocation loops and stacking faults in both irradiated and control samples, which would have made it more difficult to detect any differences if these were present. A theoretical analysis of the merits of this technique indicates that, although at high magnification it is potentially sufficiently sensitive to detect point defects, confidence in the analysis (i.e. high representativeness) would require low magnification, making detection of defects in the expected concentrations difficult.
- Positron annihilation measurements indicate that there is no detectable change in the population or nature of defects after gamma irradiation. However, like HR-TEM, it also indicated a high concentration of dislocations in both samples, which would have made it more difficult to detect any differences if these were present. A theoretical analysis of the merits of this technique indicates that, although it has high "representativeness" (large volume of material probed), the sensitivity required to measure a level of damage commensurate to that expected in the copper containers on the basis of current theoretical predictions is beyond the current capabilities of the technique.
- Electrical resistivity measurements showed no detectable change between the irradiated and the unirradiated samples. A theoretical analysis of the merit of these measurements indicates that it is unlikely to have sufficient sensitivity to detect changes at the concentrations expected.
- Nanoindentation showed no detectable difference in hardness and modulus between irradiated and unirradiated samples. Correlating the results of these measurements with defect types and at the concentrations expected is likely to be even more difficult than other techniques and would require use of samples with lower initial defect density as well as larger grain size. On the other hand, the lack of changes observed with this technique provides a direct indication that "static" mechanical properties were not affected by the irradiation.

A theoretical analysis of the point defect densities expected to be generated by gamma irradiation in this experiment (25 °C) and the real application (< 90 °C) indicates that, due to thermal annealing effects, the likely maximum defect concentrations are much below the capability of current state-of-the-art techniques, making the task of measuring the concentration of such defects beyond reach. Further work could consider the use of well-annealed samples and whether the use of even higher dose rates and cryogenic temperatures during and after irradiation would make the detection of such defect concentrations possible.



## List of abbreviations and units

BF	Bright Field
BWR	Boiling Water Reactor
Cu-OFP	Oxygen Free Phosphorous Doped Copper
DF	Dark Field
DVM	Digital VoltMeter
eV	electron Volt
EDS	Energy Dispersive X-ray Spectrometer
FEG	Field Emission Gun
FIB	Focused Ion Beam
HAADF	High-Angle Annular Dark-Field
HR-STEM	High Resolution Scanning Transmission Electron Microscopy
HR-TEM	High Resolution Transmission Electron Microscopy
IACS	International Annealed Copper Standard
KBS-3	KBS-3 concept for geological disposal of spent nuclear fuel
NPL	National Physical Laboratory
PALS	Positron Annihilation Lifetime Spectroscopy
RIS	Radiation-Induced Segregation
SATW	Super Atmospheric Thin Window
SEM	Scanning Electron Microscopy
SKB	Svensk Kärnbränslehantering AB (Swedish Nuclear Fuel and Waste Management Co)
TEM	Transmission Electron Microscopy





# Contents

<b>1</b>	<b>Introduction</b>	9
1.1	Background	9
1.2	Objectives	10
1.3	Approach and Scope	10
1.4	Structure of the document	10
<b>2</b>	<b>Experimental methods</b>	11
2.1	Materials	11
2.2	Preparation, irradiation and handling of samples	11
2.2.1	Sample preparation	11
2.2.2	Irradiation	11
2.2.3	Delivery of the samples to testing facilities	12
2.3	Positron Annihilation Lifetime Spectroscopy (PALS)	12
2.4	High-Resolution Transmission Electron Microscopy (HR-TEM)	14
2.5	Nanoindentation measurements	14
2.6	Resistivity measurements	14
<b>3</b>	<b>Results</b>	17
3.1	PALS	17
3.2	HR-TEM	18
3.2.1	Low magnification	18
3.2.2	High magnification	18
3.3	Nanoindentation	20
3.3.1	Hardness versus displacement	20
3.3.2	Modulus versus displacement	21
3.4	Electrical resistivity	21
<b>4</b>	<b>Discussion</b>	23
4.1	Initial state of the material	23
4.2	Effect of thermal annealing	24
4.3	Effect of dose rate	25
4.4	Effect of gamma energy	25
4.5	Concentration of point defects due to gamma irradiation	26
4.6	Concentration of point defects due to neutron irradiation	28
4.7	Sensitivity of experimental techniques	29
4.7.1	HR-TEM	29
4.7.2	PALS	30
4.7.3	Nanoindentation measurements	30
4.7.4	Electrical resistivity	30
4.8	Changes in mechanical properties	31
<b>5</b>	<b>Conclusions</b>	33
	<b>References</b>	35
	<b>Appendix A</b> Radiation Certificate	37
	<b>Appendix B</b> Damage Calculations	39



# 1 Introduction

## 1.1 Background

In the Swedish KBS-3 concept for disposal of spent nuclear fuel, the fuel elements are placed in copper-cast iron canisters, which are embedded in compact bentonite clay in a repository built in a granitic formation at approximately 500 m depth. The assessment of the long-term safety of such a repository, with regards to radionuclide concentration and dose in the surface biosphere, relies, among several other factors, on the evaluation of various degradation mechanisms for the canister. While the cast iron insert gives the canister structural integrity and the strength to withstand high loads due to, e.g. swelling of the bentonite clay or future glaciation, the copper shell serves as a corrosion barrier, protecting the iron insert and the fuel elements from ground water.

The copper used in the fabrication of the KBS-3 canisters is an oxygen-free phosphorus doped copper (Cu-OFP). Oxygen-free means that the copper contains less than 5 wt.ppm oxygen, which makes it resistant to hydrogen embrittlement via the reduction of oxides in the material. The addition of 30–70 wt.ppm elemental phosphorus gives the material improved deformation properties in terms of enhanced creep ductility (Sandström and Wu 2013). This is to minimise the risk that the copper shell ruptures if the copper-cast iron canister is slightly deformed by small movements in the host rock.

One factor that needs to be accounted for in the evaluation of degradation mechanisms of the canister materials is the radiation field from the encapsulated spent fuel. Both the cast iron insert and the copper shell absorb limited doses of both neutron and gamma radiation from the radioactive decay of the spent fuel. The radiation fields affecting the canister materials have been examined in several reports, and the material damage due to irradiation has been computed from these fields and the displacement damage energy cross-sections for the materials. Guinan (2001) calculated that the initial damage rate in copper (shielded by the cast iron insert) due to gamma radiation from the spent fuel is about  $1.7 \times 10^{-10}$  dpa/year<sup>1</sup>. Accounting for the decay of the gamma source, Guinan's calculations predicted that this integrates to an accumulated damage of  $4 \times 10^{-9}$  dpa in  $10^5$  years (the time it takes for the radioactivity of the spent fuel to reach the level of natural uranium ore). Although this number is small, the actual damage due to gamma radiation might be even smaller, since the effect of thermal annealing was not explicitly taken into account by Guinan. In the repository, the copper shell will have an initial temperature of 70 °C, which then increases and peaks at 95 °C after a decade, and then slowly decreases back to 50 °C in circa 500 years. Of the total gamma dose of circa 100 kGy, 99.9 % is absorbed during the first few hundred years, meaning that thermal annealing should have a significant effect on the accumulation of damage due to gamma radiation, the effect of which is addressed quantitatively in this report.

As discussed by Guinan, the predicted accumulation of damage of circa  $10^{-9}$  dpa in  $10^5$  years due to gamma (as well as the larger effect of  $10^{-7}$  dpa due to neutron damage), is orders of magnitude below what has been found to give measurable effects on the yield stress of copper. It was therefore predicted that the gamma dose absorbed by the copper shell in the spent fuel canister should have negligible effects on the mechanical properties of the material. Furthermore, since the accumulated damage due to gamma is so small, and the concentration of any impurities in the material are already very low (one hundred at.ppm at most), it was further predicted that the accumulated damage would not affect the distribution of impurities, e.g. phosphorus.

In this work, we aim to verify the predictions of negligible radiation damage in the copper canister due to gamma radiation. While aware of that the predicted accumulated damage of  $10^{-9}$  dpa is not measurable, we aim to verify that the damage accumulated after 100 kGy gamma-irradiation, is below the sensitivity of the applied methods. The approach is to compare irradiated and non-irradiated material, with respect to changes in the defect structure or material properties. This is done by direct analysis of material defects by Positron Annihilation Lifetime Spectroscopy (PALS) and High-Resolution Transmission Electron Microscopy (HR-TEM), but also by measuring material properties that could be affected by significant radiation damage, i.e. material hardness by nanoindentation, and electrical resistivity.

---

<sup>1</sup> Note that Guinan reports a damage rate of  $1.07 \times 10^{-10}$  dpa year<sup>-1</sup> on page 19 and a damage rate of  $1.7 \times 10^{-10}$  dpa year<sup>-1</sup> on page 20. In this document we use a damage rate of  $1.7 \times 10^{-10}$  dpa year<sup>-1</sup>.

## 1.2 Objectives

The objective of this work is to develop an understanding of the effect of gamma radiation on the microstructural and material properties of pure copper (as a proxy for Cu-OFP) at doses relevant for disposal of spent nuclear fuel in the KBS-3 concept, thus evaluating the conclusions of the modelling study described in Guinan (2001).

## 1.3 Approach and Scope

In order to meet the objectives of the work, a research team at Wood designed an experimental programme to investigate the effects of gamma radiation on the microstructure of copper using cutting edge, high resolution techniques. The techniques employed included:

- High-Resolution Transmission Electron Microscopy (HR-TEM).
- Positron Annihilation Lifetime Spectroscopy (PALS).
- Electrical resistivity.
- Nanoindentation.

In discussion with SKB, and in light of the very small scale and concentrations of any point defects that may be generated by gamma radiation (damage of the order of  $10^{-10}$ – $10^{-9}$  dpa reported by Guinan (2001) after 100,000 years), Wood designed an exploratory programme, aimed at carrying out an initial characterisation of defects that may be generated in high purity copper at doses of relevance to the KBS-3 concept. High purity copper was used in place of Cu-OFP to reduce complexities in interpretation that could be associated with the effect of chemical impurities (particularly phosphorous) on the measurements carried out in this study.

Additionally, in the absence of detailed information about the microstructure of commercially-available materials, to complete the experimental programme over relatively short timescales, and in light of the exploratory nature of the planned activities, annealing of the samples was not planned (nor implemented) in this work. One advantage of the approach was that the work was carried out on cold-worked copper, which is expected to mimic more accurately the condition (i.e. residual cold work) of the outer machined surface of the KBS-3 copper canister. On the other hand, the relatively high defect density initially present in the metal resulted in reduced possibilities to observe any changes associated with gamma irradiation.

Beyond the experimental work, theoretical work was carried out to discuss the expected concentration of point defects in the conditions of interest. Based on that, the sensitivity of different techniques and their ability to probe a sufficiently high volume of material to yield confidence in the observations (i.e. “representativeness”) was discussed.

## 1.4 Structure of the document

The structure of the document is as follows:

- Chapter 2 describes the experimental approach, including the materials and methods used for this project. This includes a detailed description of the irradiation and of the analytical techniques used to characterise irradiated and control samples.
- Chapter 3 presents the results of the experimental work on a technique-by-technique basis, starting with the microstructural measurements (PALS and HR-TEM) and followed by static mechanical properties and electrical resistivity measurements.
- Chapter 4 contains a discussion and interpretation of the experimental results, including considerations on the expected concentrations of point defects and required sensitivity and “representativeness” of different techniques.
- Chapter 5 presents the main conclusions of the study.

## 2 Experimental methods

### 2.1 Materials

For this work ultra-pure oxygen free copper rods were acquired from Goodfellow. These were as-drawn rods of 100 mm length and 5.0 mm diameter of 99.999 % purity (5N) (product code: CU007945).

### 2.2 Preparation, irradiation and handling of samples

#### 2.2.1 Sample preparation

The copper rods were cleaned using a 5 % citric acid pickling procedure. They were then kept under an Ar atmosphere prior to being encapsulated, under Ar, in glass ampules. The glass ampules were then brought to Wood's Harwell Irradiation Facility for irradiation. Half of the ampules were irradiated, and half were kept unirradiated in similar environmental conditions to provide suitable control samples.

#### 2.2.2 Irradiation

Gamma irradiation was performed in an irradiation cell containing a  $^{60}\text{Co}$  source, which has an energy spectrum with  $\gamma$  peaks at 1.1732 and 1.3325 MeV. Wood operates a dry, walk in gamma irradiation facility which utilises four  $^{60}\text{Co}$  sources, sealed within tubes and mounted in a square arrangement. The glass ampules (including spares) were arranged in a circular array around one of the  $^{60}\text{Co}$  sources with a consistent radius around the centre line of the source as shown in Figure 2-1.

Once securely positioned, the copper samples were irradiated at an average dose rate of 955 Gy/h to a total dose of 109 kGy at the ambient temperature of the facility (about 22 °C). The aim was to achieve a total estimated dose of 100 kGy (comparable to the full repository dose) over a few days, to enable the work to be completed over a short period of time. It should be noted that this dose rate (ca 1 kGy/h) is several orders of magnitude higher than that expected under repository conditions (< 0.5 Gy/h at start and decreasing). Considerations on the impact of the dose rate and gamma energies used are provided in sections 4.3 and 4.4. The irradiation was successfully completed without issue over a five-day period (30 August – 4 September 2018) and was only interrupted briefly to rotate the samples to ensure a uniform dose was achieved. A full radiation certificate providing detail on the irradiation conditions is provided in Appendix A.

The radiation dose rate was measured directly by a type 2581 thimble ionisation chamber (serial number 1408) connected to a Thermo Electron Corporation Farmer dosimeter (type 2570/1B, serial number 1361), both calibrated to UK national standards by NPL. This method of dosimetry offers a real time measurement of the dose rate to the samples and is more accurate than commonly used secondary methods that rely on changes in optical properties of the dosimeter material.

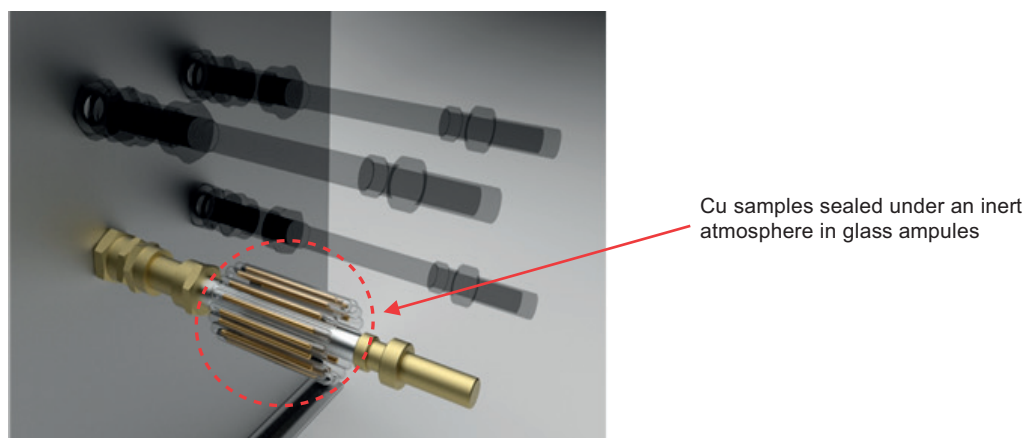


**Figure 2-1.** Schematic diagram of samples configuration during irradiation, showing the tubular  $^{60}\text{Co}$  source around which samples were irradiated.

### 2.2.3 Delivery of the samples to testing facilities

Once irradiation had been completed, the samples, irradiated and unirradiated, were brought by members of the Wood team to specific research facilities and handed over in person, to ensure samples were correctly handled. Post-irradiation characterisation was carried out a 15–60 days from the completion of the irradiation. This was done to keep the time for annealing processes to occur reasonably low. The length of times lapsed after the irradiation and before different characterisation experiments were performed is provided in Table 2-1. The analysis reported in Section 4.2 indicates that much smaller timescale may be sufficient for annealing processes to operate on single point defects. Nevertheless, the work was carried out to confirm the analysis experimentally.

**Table 2-1. Length of time after irradiation, before characterisation experiments were performed.**

	Date of irradiation	Date of analysis	Time elapsed since end of irradiation (days)
PALS	30 August – 4 September 2018	17 and 28 September 2019	~15–25
HR-TEM	30 August – 4 September 2018	19 September and 31 October 2018	~15–60
Nano-indentation	30 August – 4 September 2018	24 September and 11–12 October 2018	~20–40
Electrical resistivity	30 August – 4 September 2018	25–28 September 2018	~20–25

## 2.3 Positron Annihilation Lifetime Spectroscopy (PALS)

Positron Annihilation Lifetime Spectroscopy (PALS) was performed by the University of Bristol. These measurements were carried out on a set of three irradiated samples and three unirradiated control samples. Positrons are bulk probes, typically penetrating hundreds of microns into the sample. Being positively charged, they are excellent probes of open-volume defects in metals.

Discs were cut from both ends of each copper rod. PALS measurements were performed on the faces of the discs which had not been cut, thus minimising any effect of surface preparation (not expected anyway, given that positrons are “bulk probes” see Section 3.1). No further preparation was made to the surface. Images of the cut discus are shown in Figure 2-2.

Positrons are obtained from a  $^{22}\text{Na}$  radioactive source and thus exhibit a typical  $\beta$ -spectrum of energies with a peak at 540 keV. The typical implantation depth of positrons into copper would be more than 100  $\mu\text{m}$ , meaning that the positrons sample the bulk material. The physical size of the source (which is deposited onto a Kapton film and sealed by Kapton tape) results in a source spot on the sample of about 3 mm radius. After being injected up to a depth of 100  $\mu\text{m}$  and becoming thermalized (within a few picoseconds), the positrons are able to diffuse up to a length of 0.1  $\mu\text{m}$  before being annihilated, typically sampling a volume containing  $10^{20}$  atoms<sup>2</sup>.

Two discs from each sample were used to sandwich a  $^{22}\text{Na}$  positron source (sealed in Kapton film). Lifetime spectra (with at least 5.4M counts) were accumulated over 24-hour periods (see Figure 2-3 for a typical spectrum). Reference spectra (using a pair of single crystal Al samples) were taken before and during the experiments to confirm spectrometer stability. The spectra were analysed in the standard manner by fitting a set of exponentials to the spectra (Giebel and Kansy 2011). Source components (due to positron annihilation within the source rather than the sample) were accounted for in the analysis and the results therefore refer to annihilation in the copper sample only. The process of extracting lifetimes and intensities, which involves fitting a series of decaying exponentials, has been very carefully developed and optimised over the past 50 years of positron annihilation experiments. The current spectra were analysed with the state-of-the-art software, “LT” (Giebel and Kansy 2011). The software confirmed that the reference measurements on Al provide an excellent check on the spectrometer stability and mathematical fitting procedures employed. The typical uncertainty in the measured lifetimes is about 3 ps.

<sup>2</sup> A lateral linear dimension of 3 mm, an injection depth of 100  $\mu\text{m}$  and a diffusion length of 0.1  $\mu\text{m}$  correspond to a volume of the order of  $2.8 \times 10^{-3} \text{ cm}^3$ . In the case of copper, a density ( $\rho$ ) of  $\sim 9 \text{ g cm}^{-3}$  and an atomic mass ( $M$ ) of  $\sim 63 \text{ g mol}^{-1}$  lead to a number of atom  $N = (\rho V N_A) / M = 10^{20}$  atoms, where  $N_A$  is Avogadro’s number ( $\sim 6 \times 10^{23} \text{ atoms mol}^{-1}$ ).



**Figure 2-2.** Discs cut from the top and bottom of each Cu rod.

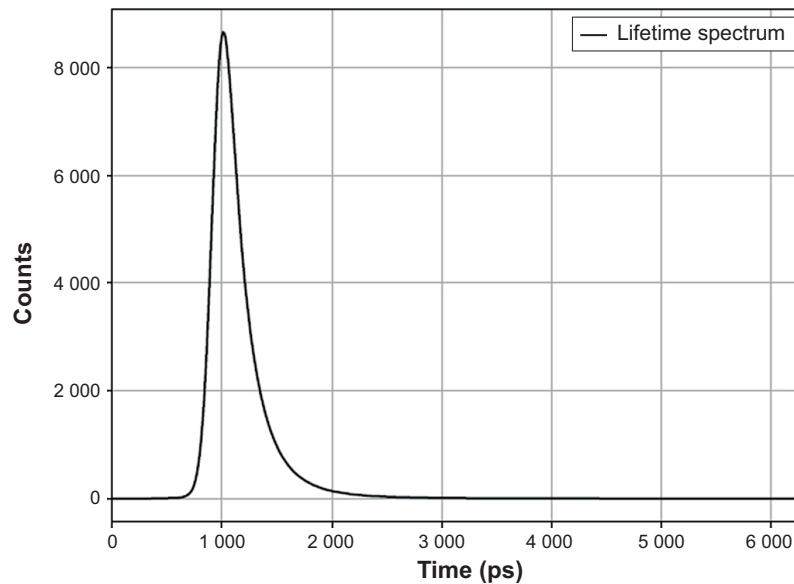


**Figure 2-3.** Example of one of the measured lifetime spectra. By fitting a series of exponentials, the fate of the positron can be inferred, and thus information about the nature of the defects and their population density can be extracted.

In a defect-free metal sample, the positron will rapidly thermalize (within a few ps) and then propagate in a Bloch state for a time which is typically of the order of 100–200 ps before annihilating with an electron producing a pair of gamma photons.

If the metal possesses defects such as vacancies, vacancy clusters or dislocations where the positive charge density is lower than elsewhere in the material, then these are likely to trap positrons. Since the lifetime of the positron is closely related to the electron density, the lower electron density in these regions results in longer positron lifetimes. At high enough concentrations of vacancies, saturation trapping occurs where all positrons that enter the sample are eventually trapped and annihilate from the trapped state. This process can be described by a so-called two-state trapping model, which results from solving coupled differential equations describing the populations of positrons in the two states (i.e. the bulk and trapped in a vacancy). The result will be two distinct lifetimes, usually denoted  $\tau_1$  and  $\tau_2$ , where  $\tau_2$  is the lifetime of the positron in the vacancy and  $\tau_1$  is a so-called “reduced bulk lifetime” reflecting the fact that positrons can be removed from the bulk by both annihilation and trapping. Note that this “reduced bulk lifetime” will be shortened from the bulk value by trapping into the defect state. If the specific trapping rate (i.e. the efficiency of a particular defect to trap positrons) is known, then this model can be used to estimate the concentration of the trapping defect.

For reference, the experimentally determined lifetime of a positron in bulk, defect-free Cu is  $\sim 120$  ps (Campillo Robles et al. 2007), while lifetimes associated with positrons trapped in monovacancies are  $\sim 180$  ps (Campillo Robles et al. 2007). While dislocations are relatively shallow traps for positrons, the accepted view is that positrons rapidly diffuse along the dislocation line until encountering a vacancy.

The lifetime associated with this “dislocation+monovacancy” trap is thought to be  $\sim 164$  ps. The lifetimes associated with clusters of vacancies are all, of course, longer than the monovacancy (positron lifetime for a divacancy in Cu is  $\sim 215$  ps) (Čížek et al. 2002). Lifetimes associated with stacking faults are only slightly longer (10–15 ps) than the bulk lifetime (Zhou et al. 2015).

## 2.4 High-Resolution Transmission Electron Microscopy (HR-TEM)

High-Resolution Transmission Electron Microscopy (HR-TEM) was performed by the University of Oxford. These measurements were carried out on a single irradiated sample and a single unirradiated control sample. A 3 mm section was cut from the middle of either rod, the cut surface was ground and polished with a succession of polishing papers down to 1 micron. The mirror polished surface from the middle of the section was then used to mill a TEM cross section with Zeiss NVision Focused Ion Beam (FIB) to an appropriate dimension for HR-TEM. The original thickness of the TEM slice was about 0.5 mm, which was then reduced to approximately 50–200 nm to achieve electron transparency.

HR-TEM was carried out with a JEOL 3000F, which is a high resolution TEM/STEM instrument with cold Field Emission Gun (FEG). The instrument is equipped with an Oxford Instruments energy dispersive X-ray spectrometer (EDS) with a super atmospheric thin window (SATW) detector, that allows chemical analysis of elements down to boron under suitable conditions.

## 2.5 Nanoindentation measurements

Nanoindentation hardness measurements were performed by the University of Oxford. In these measurements the term “nano” refers to the sensitivity of the measurements in the direction perpendicular to the surface probed (z-direction) rather than to the lateral resolution of the technique (i.e. xy plane). The lateral size of the indents is 14 microns, yielding a comparable lateral resolution (i.e. a resolution of the order of 10  $\mu\text{m}$  in the xy plane). The nanoindenter produces a force vs. displacement function either continuously or in load and unload cycles. In this respect, the approach is different from that employed in micro-hardness measurements, in which examination of the size of the indent after the load has been removed is required. Hence, in micro-hardness measurements, there is no measure of an elastic recovery, which can be, conversely, measured under nanoindentation. Nanoindentation can thus be used to infer not only values of the hardness but also the elastic module of a material.

Nanoindentation measurements were carried out on a single irradiated sample and a single unirradiated control sample. From each sample, a number of cross sections were analysed. The samples for nano-indentation were prepared by sawing a slice from each rod and polishing to a mirror finish with colloidal silica. A slow cut (Loadpoint) diamond saw was used to minimise damage but any saw damage would have been removed during the polishing process. Indents were performed across the diameter of the disk obtained after cutting. The cutting process is expected to have resulted in some changes in the surface properties. However, the same process was used in preparation of both irradiated and unirradiated samples, thus allowing a direct comparison between the results.

Nanoindentation hardness measurements were performed with an MTS Nanoindenter XP using a 14  $\mu\text{m}$  Berkovich indenter at a strain rate of  $0.05 \text{ s}^{-1}$  with a 2  $\mu\text{m}$  target indent depth, which equates to an approximate load of 125 mN. The hardness and modulus were measured continuously through the loading cycle using the continuous stiffness method, which superimposes a 2 nm oscillation over the load cycle. The indenter was calibrated using the Oliver-Pharr Method against fused silica (Oliver and Pharr 1992).

## 2.6 Resistivity measurements

DC resistivity measurements were carried out at the National Physical Laboratory (NPL) in Teddington, UK. DC measurements were chosen as it allows the determination of the material’s bulk resistivity, whereas AC techniques give surface-specific information. These measurements were carried out on a set of three irradiated samples and three unirradiated control samples.



The measurements were carried out at room temperature using a four-point probe technique. The set-up can be seen in Figure 2-4. For these measurements, two brass connectors were placed in contact with either side of the sample, which have an approximate length of 100 mm, and a current of 1 A applied. A pair of knife edges, with a nominal separation of 50 mm, were placed in contact with the sample and the potential was measured across the knife edges.

The resistivity,  $\rho$  (Ohm m), can then be calculated using the formula described in Equation 2-1, where  $R$  is the electrical resistance (Ohm),  $A$  is the cross-sectional area of the sample ( $\text{m}^2$ ) and  $L$  is the length of the path across which the potential drop is measured (m), in this case 50 mm. The conductivity,  $\sigma$  (S/m) can then be determined from the resistivity according to Equation 2-1.

$$\rho = \frac{RA}{L} \quad \text{Equation 2-1}$$

$$\sigma = \frac{1}{\rho} \quad \text{Equation 2-2}$$

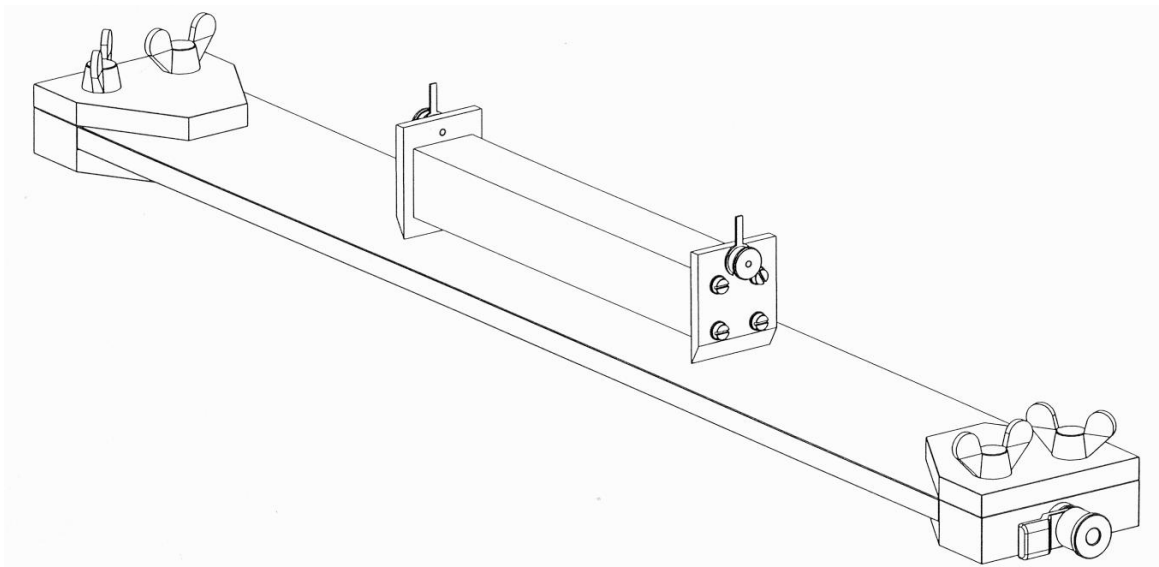


**Figure 2-4.** DC conductivity measurement set-up (four-point probe technique) on a plate-shaped sample. The image shows the brass connectors of which the current is applied (sample edges), and the knife-edges on which the resulting potential is measured (the central area).



## 3 Results

### 3.1 PALS

The results of PALS measurements on irradiated and unirradiated samples are presented below. An example raw spectrum measured on one of the samples was shown in Figure 2-3. Although all samples measured had slightly different sets of lifetime components, most likely due to the slightly different defect compositions of the raw materials, there was no difference detectable between the sets of pristine and irradiated samples. This can be seen in Figure 3-1, where a difference between normalised lifetime spectra (having summed together all the data on unirradiated and  $\gamma$ -irradiated samples separately and then subtracted the two datasets from each other) is shown. For comparison, the same parameter is plotted for an ion-irradiation experiment on tungsten (carried out with vanadium ions) where the difference is clear. This comparison indicates that no differences in the spectrum of  $\gamma$ -irradiated and unirradiated copper samples can be ascertained (the signal visible around 1000 ps is expected to be noise). In fact, there was no difference between any of the spectra.

Using conventional deconvolution methods, the signal obtained with these measurements can be deconvoluted to yield characteristic lifetimes ( $\tau$ ) and intensities ( $I$ ). The lifetimes and intensities resulting from this process are shown in Table 3-1. By convention, the shortest lifetime is referred to as  $\tau_1$  and has an intensity  $I_1$ , and so on. In this case, spectra from all the samples could be fitted with two components, which we associate (see Discussion in chapter 4 below) to a very short “reduced bulk” lifetime ( $\tau_1$ ) and a longer lifetime associated with positrons trapped at dislocations ( $\tau_2$ ). The fact that a “reduced bulk” lifetime with a relatively low intensity  $I_1$  is observed shows that not all the positrons are being trapped in defects, i.e. the samples are close to, but have not quite reached, saturation trapping (a small number are still annihilating from the bulk). This means that we are not working at the saturation of the technique, i.e. an increase in defect concentration would result in an increase in the proportion of positrons trapped. The uncertainty on the shorter lifetimes is typically a few ps.

**Table 3-1. Lifetime and intensities found in different samples. The uncertainty in the shorter lifetimes is typically a few ps.**

Sample no.	Irradiated?	$\tau_1$ (ps)	$I_1$ (%)	$\tau_2$ (ps)	$I_2$ (%)
3	Y	28	4	170	96
4	Y	18	6	167	94
5	Y	38	5	169	95
19	N	24	6	169	94
20	N	24	5	169	95
21	N	44	4	170	96

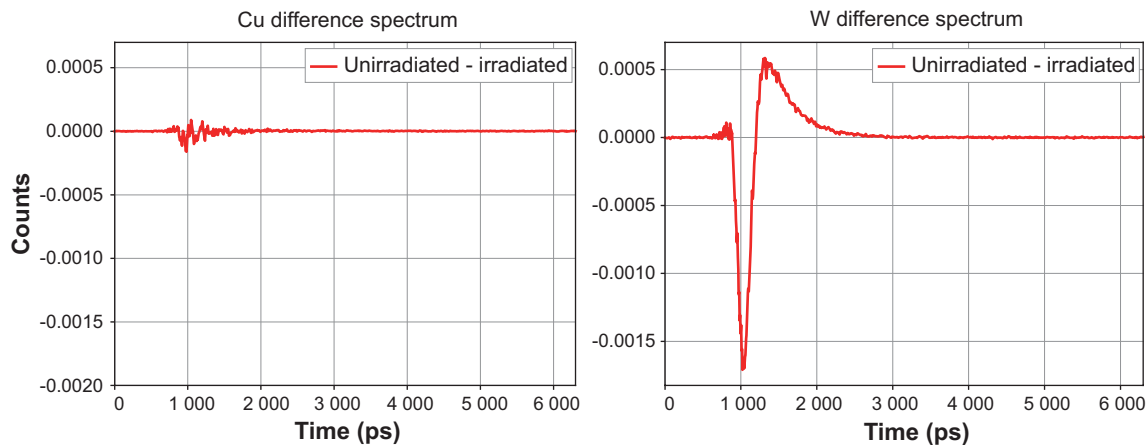


**Figure 3-1.** Difference between lifetime spectra on irradiated and unirradiated samples. Left: copper samples considered in this report. Right: For comparison, the equivalent difference spectrum for pristine and vanadium-ion irradiated tungsten is plotted. Note that the only interval where signal is collected for these samples is between 0 and 3000 ps. The spectrum is shown to 6000 ps to show that there are no “long time” time signals, associated with the presence of large voids in the samples.

## 3.2 HR-TEM

### 3.2.1 Low magnification

Low magnification micrographs of both irradiated and unirradiated samples analysed with TEM are shown in Figure 3-2. Both samples showed relatively fine grain sizes (in the hundreds of nanometres range). The main orientation of grains was similar within each of the samples but different between different samples. As a result, a high degree of confidence in the comparison between the irradiated and the unirradiated sample is not currently possible. In order to attempt to quantify any possible defect distribution additional samples or sample areas would need to be examined.

There is no obvious difference in the defect types or distribution of defects in Figure 3-2. However, the contrast of small defects depends on grain orientation and, as a result, the analysis presented is not fully conclusive.

### 3.2.2 High magnification

High magnification micrographs of both irradiated and unirradiated samples analysed with HR-TEM are shown in Figure 3-3 and Figure 3-4, in both bright field and dark field mode. Bright Field mode allows to visualise defects in the crystal due to difference in scattering abilities, according to the atomic number as well as diffraction related contrast due to changes in lattice constant (strain). The technique in dark field mode uses just one or more diffracted beam and is used to identify defects. No obvious difference is visible between irradiated and non-irradiated samples, as seen in the TEM micrographs of the irradiated sample 1 in Figure 3-3 and the unirradiated sample 17 in Figure 3-4.

Both samples showed small defects (< 10 nm) such as stacking faults and or dislocation loops. These types of defects have similar contrast sizes to vacancies or interstitial atoms. As such, distinction between the different types of defects is only possible under certain diffraction conditions, which would require the analysis of a greater number of samples.

A visual estimate of small defect numbers in sample 1 and 17 shows an average distance between defects of 5 to > 20 nm. This converts to a defect density of  $10^{22}$ – $10^{24}$  m<sup>-3</sup>.<sup>3</sup> This number is much

<sup>3</sup> The number of visible/projected changes of contrast that can correlate with small defects varies between 25 and 100 (in some areas up to 400) in an area of  $100 \times 100$  nm<sup>2</sup> with an assumed minimum estimated thickness of the TEM slice (50 nm). This correlates to approximately  $5 \times 10^{22}$  to  $8 \times 10^{23}$  defects per cubic metre. The number would decrease to  $\sim 1 \times 10^{22}$  to  $2 \times 10^{23}$  defects per cubic metre if, instead, we assume the maximum estimated thickness of the TEM slice (200 nm).

higher than the concentration of defects that would have been introduced by  $\gamma$ -irradiation according to the predictions of Guinan (2001) ( $\sim 10^{20} \text{ m}^{-3}$ ).<sup>4</sup> As a result, in order to detect vacancies or any other small ( $< 10 \text{ nm}$ ) defects that may be introduced by  $\gamma$ -irradiation, the intrinsic small defect density would need to be reduced by at least 3–5 orders of magnitude.

The dislocation density in both unirradiated and irradiated samples was estimated to be between  $4 \times 10^{14}$ – $6 \times 10^{14} \text{ (m/m}^3\text{)}$ , i.e.  $\sim 0.5 \times 10^{15} \text{ m}^2$ . In order to improve the sensitivity, the contrast overlap between extended dislocations and irradiation-induced point defects can be reduced by a careful choice of imaging conditions. Since dislocations can act as sinks for vacancies, a reduction in dislocation density would aid in the detection of any point defects generated by  $\gamma$ -irradiation.

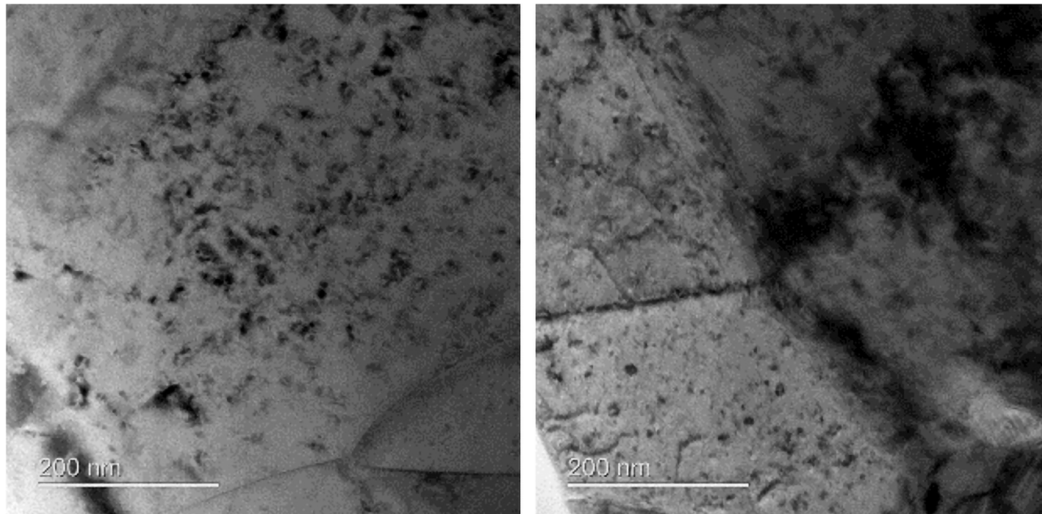


**Figure 3-2.** Low magnification TEM micrographs. Left: irradiated sample 1. Right: unirradiated sample 17.

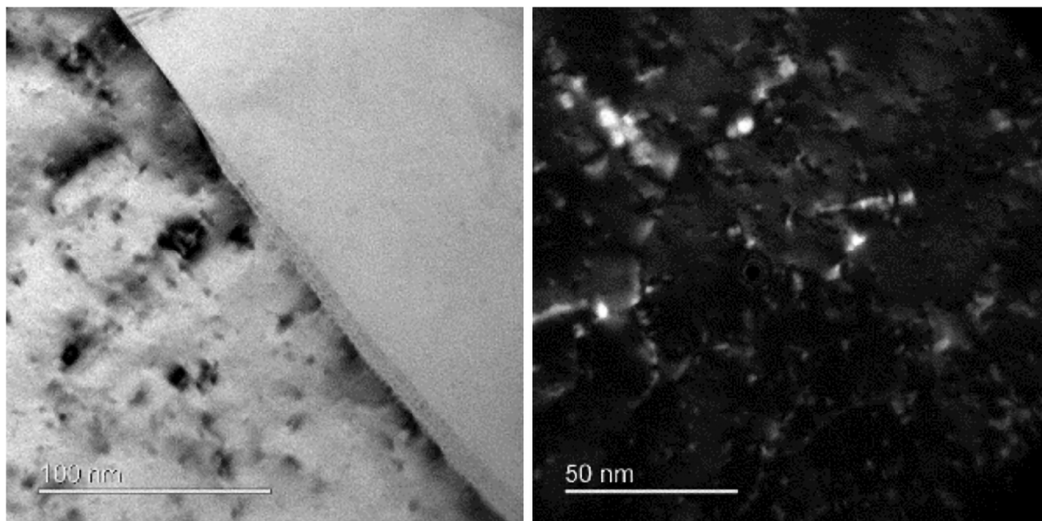


**Figure 3-3.** High magnification TEM micrographs of irradiated sample 1

<sup>4</sup> With a density ( $\rho$ ) of  $\sim 9 \text{ g cm}^{-3}$  and an atomic mass ( $M$ ) of  $\sim 63 \text{ g mol}^{-1}$ ,  $1 \text{ cm}^3$  of copper contains a number of atoms  $N = (\rho V N_A) / M \sim 10^{23}$  atoms, where  $N_A$  is Avogadro's number ( $\sim 6 \times 10^{23} \text{ atoms mol}^{-1}$ ). A defect concentration  $[D]_A$  per atom of  $4 \times 10^{-9} \text{ (atom}^{-1}\text{)}$ , reported by Guinan after the full dose, is equivalent to a volumetric defect concentration  $[D]_V = [D]_A \times N \sim (4 \times 10^{-9} \times 10^{23}) \text{ cm}^{-3} = 4 \times 10^{14} \text{ cm}^{-3} = 4 \times 10^{20} \text{ m}^{-3}$ .

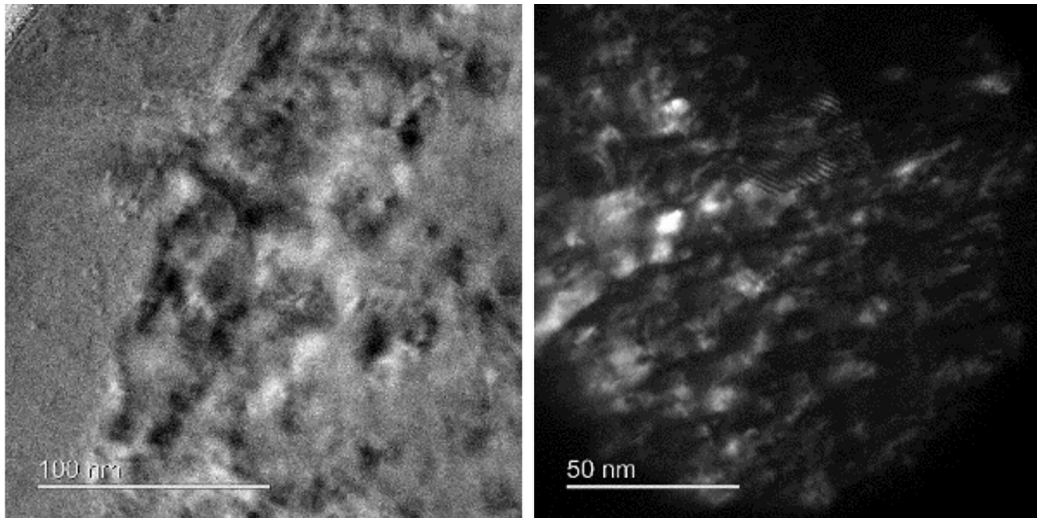


Figure 3-4. High magnification TEM micrographs of unirradiated sample 17

### 3.3 Nanoindentation

Hardness and modulus curves from nanoindentation of the polished copper surfaces are shown in Figure 3-5 and Figure 3-6 respectively. A set displacement of 2 000 nm is prescribed in these measurements, thus penetrating somewhat in the “bulk” of the metal. Error bars are  $\pm 1$  standard deviation.

Essentially there is no discernible difference in neither hardness nor modulus between the irradiated and un-irradiated reference samples. From the microstructure observed in the HR-TEM study (grain size of the order of 100 nm) it is likely that, for both hardness and modulus, the effects of grain boundaries would exceed those of any radiation-induced defects (the lateral size of the indents and, as a result, the lateral resolution of the technique is 14 microns). In principle, measurements on different samples (as well as repeated measurements in the same sample) could be made in search of systematic differences in modulus, but this could be due to crystallographic orientation of the specific grains probed rather than due to other factors (the modulus in copper varies by nearly a factor of 3 between the  $\langle 100 \rangle$  and  $\langle 111 \rangle$  directions). Given the small grain size of the material tested in this case, however, such variations would not be expected.

#### 3.3.1 Hardness versus displacement

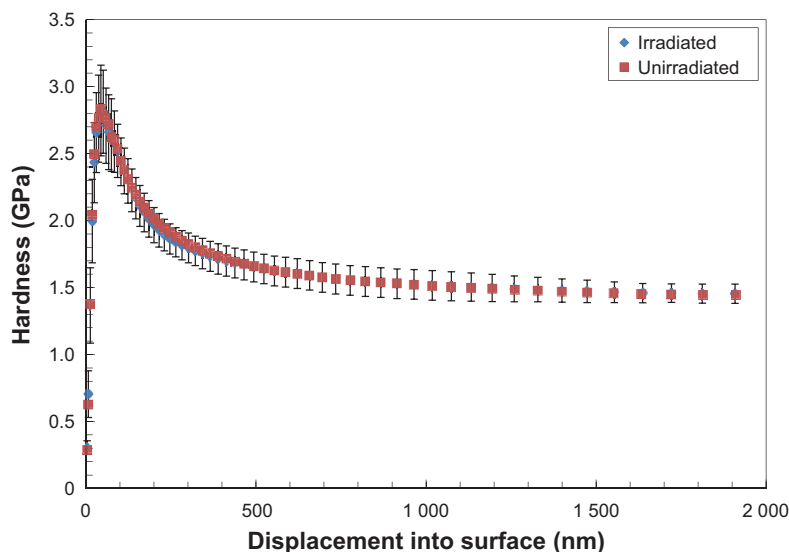
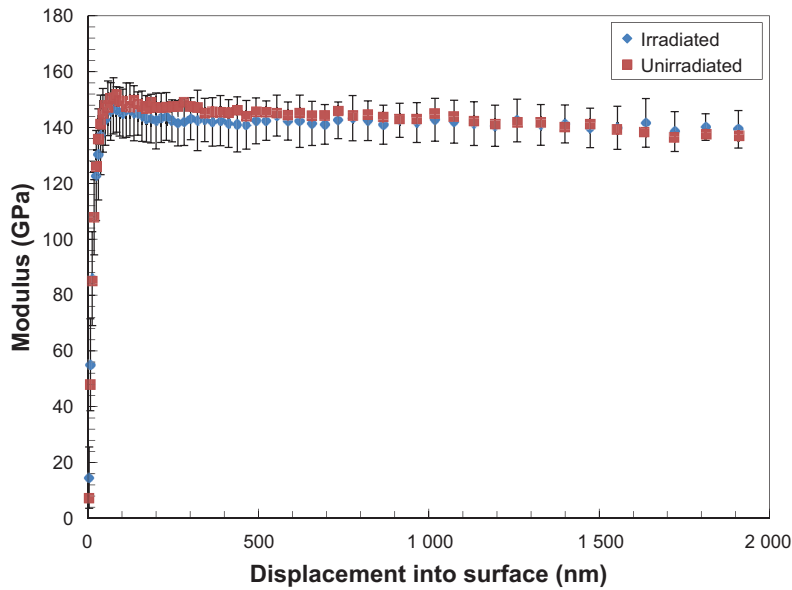


Figure 3-5. Hardness versus displacement of indenter tip. Error bars displayed for the irradiated sample only but were found to be a similar size for unirradiated material.

### 3.3.2 Modulus versus displacement



*Figure 3-6. Modulus versus displacement of indenter tip. Error bars displayed for the irradiated sample only but were found to be a similar size for unirradiated material.*

### 3.4 Electrical resistivity

The resistivity and conductivity values for all samples are shown in Table 3-2. The conductivity is reported both in SI (MS/m) and percentage of Industry Annealed Copper Standard (%IACS), which is based on the electrical conductivity of “commercially-pure” copper (i.e. 100 %IACS is equal to 58 MS/m)<sup>5</sup>.

In these measurements, the expanded uncertainty was determined through a theoretical analysis of different contributors as opposed to directly measured through repeats of the same measurements. Specifically, the expanded measurement uncertainty was determined by combining the standard uncertainty for each source of uncertainty in the measurement and multiplying it by a coverage factor,  $k$ . The coverage factor determines the confidence in the quoted value. For example, in a Gaussian or normal probability distribution, 67 % of the data is expected to be within one standard uncertainty of the mean, while 95 % of the data is expected to be within two standard uncertainties. In these measurements, to have a confidence of 95 % in the quoted value, a coverage factor of  $k = 2$  is used.

**Table 3-2. Resistivity and conductivity values for the irradiated and unirradiated copper samples. The reported expanded uncertainties provide a coverage probability of approximately 95 %.**

Sample ID	Resistivity (nΩm)	Conductivity (MS/m)	Conductivity (%IACS)	Expanded uncertainty (± % of measured value)
<b>Irradiated Samples</b>				
6	17.07	58.57	100.98	0.30
7	17.07	58.59	101.02	0.30
8	17.06	58.64	101.10	0.30
<b>Unirradiated Samples</b>				
22	17.06	58.61	101.04	0.30
23	17.04	58.68	101.17	0.30
24	17.05	58.64	101.11	0.30

<sup>5</sup> Note that modern high-purity, well-annealed copper can achieve a conductivity of about 103 % IACS.

The individual uncertainty contribution used for the expanded uncertainty are shown in the uncertainty budget in Table 3-3. Here the divisor is determined by the probability distribution,  $c_i$  is the sensitivity coefficient which is used to determine the standard uncertainty, and  $u_i$  and  $V_i/V_{\text{eff}}$  are the degrees of freedom which are used to assess whether the distribution of the combined uncertainty is normal, and thus to determine whether a coverage factor of  $k = 2$  can be used. More information on the expression and determination can be found in ISO (2008) and UKAS (2007).

**Table 3-3. Expanded resistivity measurement uncertainty.**

Uncertainty in measurement of resistivity, $\rho$						
Source of uncertainty	Value $\pm$ %	Probability distribution	Divisor	$c_i$	$u_i$ $\pm$ %	$V_i$ or $V_{\text{eff}}$
<b>Current measurement</b>						
0.1 $\Omega$ for current measurement	0.007	normal	1	1	0.0070	inf.
Calibration of DVM (current)	0.0500	normal	2	1	0.0250	inf.
Resolution of DVM	0.0502	rectangular	1.732051	1	0.0290	inf.
<b>Nanovoltmeter output</b>						
Calibration of DVM (nanovoltmeter)	0.050	normal	2	1	0.0250	inf.
Resolution of DVM	0.0117	rectangular	1.732051	1	0.0068	inf.
Calibration of nanovoltmeter	0.1576	normal	2.18	1	0.0723	15
<b>Dimensions</b>						
Calibration of micrometre	0.020	normal	2	1	0.0100	inf.
Repeatability of rod diameter	0.0190	normal	1	1	0.0190	9
Resolution of micrometre	0.0099	rectangular	1.732051	1	0.0057	inf.
Calibration of digital Vernier calliper	0.0203	normal	2	1	0.0102	inf.
Repeatability of knife edge length	0.0070	normal	1	1	0.0070	9
Resolution of digital Vernier calliper	0.0100	rectangular	1.732051	1	0.0058	inf.
<b>Measurement</b>						
Temperature Stability	0.0410	rectangular	1.732051	1	0.0236	inf.
Contact resistance	0.2	rectangular	1.732051	1	0.1155	inf.
Repeatability of measurement	0.0099	normal	1	1	0.0099	4
<b>Combined Uncertainty</b>					0.1486	265
<b>Expanded Uncertainty</b>		normal	$k = 2$		0.2972	

Expanded Uncertainty rounded to  $\pm 0.30$  %,  $k = 2$

The average resistivity and conductivity for the irradiated samples are 17.07  $n\Omega m$  and 58.60 MS/m respectively, while the average resistivity and conductivity for the unirradiated samples are 17.05  $n\Omega m$  and 58.64 MS/m respectively. The differences between these values are well within the experimental uncertainties determined theoretically, indicating that no discernible differences were ascertained between the samples.



## 4 Discussion

### 4.1 Initial state of the material

The results of TEM indicate that the material tested contains a high density of dislocations (approximately  $0.5 \times 10^{15} \text{ m}^{-2}$ , see Section 3.2.2), dislocation loops and stacking faults. Both extended dislocations and small dislocation loops can potentially act as sinks for irradiation-induced defects and would need to be reduced in order to increase the possibilities of obtaining a quantitative determination of potential irradiation effects. The level of cold working in the samples tested is expected to be higher than what found in the real application (modest level of cold working near the outer surface), so reducing the dislocation density to values more similar to that of annealed or lightly cold worked samples may produce a more representative material.

The high dislocation density present in the material is confirmed by PALS measurements (detecting a substantial intensity of trapping sites with decay times characteristics of dislocations in copper). The bulk lifetime for well-annealed Cu is 120 ps (Campillo Robles et al. 2007) and thus a value of  $\tau_1$  close to this, and a large intensity of this component of the spectrum ( $I_1$ ), would indicate that the majority of positrons are annihilating from the bulk. In the current set of experiments (Table 3-1),  $\tau_1$  is significantly different from that experienced in well-annealed copper and its intensity is very small, indicating that almost all the positrons are being trapped<sup>6</sup>. The second lifetime component ( $\tau_2$ ) at  $\sim 168$  ps, however, is close to a value (164 ps) typically associated with dislocations in Cu (Čížek et al. 2002)<sup>7</sup>. In general, the results obtained in the tests indicate that similar populations of dislocations are present in *all* the samples, i.e. the nature and population of defects does not appear to be connected with whether or not the samples have been irradiated. A simple two-state trapping model analysis indicates a dislocation density of  $\sim 0.9 - 1.2 \times 10^{15} \text{ m}^{-2}$  (using a specific positron trapping rate for dislocations of  $0.6 \times 10^{-4} \text{ m}^2 \text{ s}^{-1}$ ) (Čížek et al. 1999), which is very similar to that estimated from HR-TEM.

Qualitatively, similar considerations apply for resistivity measurements. For a modern high-purity copper, a resistivity of about 100–101 % IACS is indicative of a material containing a substantial number of crystalline defects (a well-annealed high-purity copper would be expected to have a conductivity of about 103 % IACS). Like HR-TEM and PALS, resistivity measurements are likely to be affected by a variety of defect types. As such, a material with a high initial concentration of dislocations and other defect types makes the observation of any defects that may be induced by  $\gamma$  radiation difficult to detect.

On the other hand, given the microstructure observed in the HR-TEM, the indentation response is likely to be dominated by grain boundaries (the crystallite size is much smaller than the lateral indent size). This suggests that the ability of this technique to study any radiation-induced effect on the material used in these tests would not only be constrained by the high density of pre-existing dislocations and other line defects (as for HR-TEM and PALS) but also by the grain size.

In summary, for all techniques employed, the presence of a high concentration of initial microstructural defects in the samples is likely to have decreased the possibility of observing any effects that may be associated with defects introduced by gamma irradiation (if any).

---

<sup>6</sup> Note that, as described in Section 2.3.1, the “reduced bulk” lifetime  $\tau_1$  is the standard name given to the component which captures the sum of annihilation rates from the bulk and trapping rate into defects; it is not the bulk lifetime (unless there is no trapping, in which case there is no  $\tau_2$ ).

<sup>7</sup> The positrons will trap at the most energetically favourable locations, and thus weak traps such as stacking faults will lose in any competition to trap positrons compared to the dislocations-monovacancy defect.

## 4.2 Effect of thermal annealing

As a result of their temperature, materials containing point defects (including irradiated materials) are subjected to defect-annealing processes. Such processes typically exhibit different temperature regimes that correspond to the loss of different types of defects to specific “sinks” (e.g. grain boundaries) by diffusion. In the case of out-of-equilibrium systems such as irradiated systems, mechanisms inducing a reduction in the concentration of defects include mutual annihilation of specific types of defect pairs (e.g. vacancies and interstitials). In these systems, the concentration of defects in conditions in which thermal annealing takes place depends on the damage rate,  $K_0$ , not the total damage. This is because radiation damage is a dynamic process, with defects being produced and lost by a variety of processes.

Experimental studies investigating microstructural defects often use electrical resistivity simultaneously with isochronal annealing to identify the major defect recovery processes. Irradiation and electrical resistivity measurements are initially conducted at very low temperature (e.g. with liquid helium, at 4 K), in a condition in which defects are immobile and thermal scattering contributions to the resistivity are minimal. The appearance of any given stage depends on the time and temperature used in the annealing experiment (and, in the case of irradiated structures, often on the time and temperature of irradiation).

Measurements of the change in electrical resistivity,  $\Delta\rho$ , as a function of annealing temperature provide information on the kinetics of defect reactions. For example, if recombination of vacancies and interstitials occurs, a decrease of  $\Delta\rho$  with temperature follows. Figure 4-1 shows a plot of the fractional change in defect concentration as a function of temperature in pure copper after electron irradiation, starting from a temperature of 4 K (Ehrhart et al. 1986). In this experiment, it was assumed that, since irradiation was conducted using electrons, only single point defects were produced. In that regard, this experiment is relevant to the study of copper canister for disposal, since in both cases the primary damage source will be Compton electrons (in the case of copper disposal canisters those generated from gamma radiation released from spent fuel).

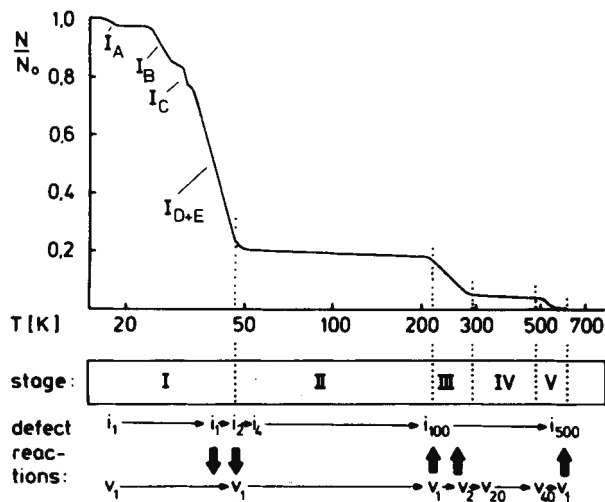


**Figure 4-1.** Annealing stages and defect reactions in pure copper after electron irradiation;  $i_1$  and  $v_1$  denote single interstitials and vacancies, respectively,  $i_2$  and  $v_2$  di-interstitials and divacancies (after Schilling et al. 1975). Time at temperature in these tests is typically 10–20 min. The concentration of defects at a specific temperature ( $N$ ), normalised to their concentration at zero Kelvin ( $N_0$ ), is proportional to changes in the resistivity measured (i.e. proportional to  $\Delta\rho / \Delta\rho_0$ ) (Ehrhart et al. 1986).

In light of the potential for annealing to affect the concentration of defects in the irradiation tests presented herein, it is informative to compare the temperatures of interest with the temperatures at which annealing processes might be at play. Thermal annealing effects could make the detection of any defect initially generated by gamma radiation more difficult (due to annihilation effects acting between irradiation and analysis). On the other hand, given that the tests were carried out at lower temperature than the real application, the concentration of defects identified in this experiment is likely to be bounding for the field exposure. This would need to be confirmed giving due consideration to the kinetics of defect generation and recovery processes, since in the real application defects would be continuously generated and annealed as opposed to be generated over short time periods and then annealed during the period before analysis, as in the experiments.

Referring back to Figure 4-1 (Was 2017, Ehrhart et al. 1986), it is important to note that, in the electron-irradiation experiments described therein, single vacancies and interstitials ( $v_1$  and  $i_1$ ) are annealed at temperatures as low as 50–200K within 10–20 minutes. These temperatures are much lower, and experienced for much shorter periods, than the temperatures in the experiment described in this study (~293 K) and the periods of time between the irradiation and the analysis (~ several weeks), let alone the expected maximum temperature and timescales of exposure of the copper canister in the field (peak temperature ~363 K for a few years). Temperatures higher than 300–500 K would be required, on the other hand, to anneal some type of defect clusters within 10–20 minute period. For the experiments presented in this report, this means that any single point defects generated during irradiation would have been annealed before the analysis was carried out, but that some defect clusters (if any were present) could have been retained within the microstructure at the time of the analysis. In the real application, due to the higher temperature of the copper shell, such defects would have also been annealed. More detailed considerations on the implications of these effects on the ability to measure defects experimentally are provided below.

### 4.3 Effect of dose rate

The dose rates employed in the measurements described in this document are many orders of magnitude higher than those expected in copper containers with encapsulated spent nuclear fuel (ca  $10^3$  Gy/h and less than 0.5 Gy/h, respectively). Given the extremely long timescales of radioactive decay of major gamma emitters in spent fuel, using higher dose rates is required to achieve, in reasonably short timescales, the total dose expected (ca 100 kGy).

Dose rate effects are expected to be important in many phenomena involving ionising radiation, for example the rates of water radiolysis and associated redox potential of resulting solutions. In microstructural studies such as those considered herein, as a result of thermal annealing, the defect density at any point in time is a function of both the temperature and the damage rate. Higher temperature and/or lower damage rate will result in a lower defect concentration. To maintain a fixed defect concentration, a higher damage rate would need to be accompanied by a higher temperature. Notwithstanding the fact that many defects (particularly single point defects) would have been annealed during the period intercurrent between the irradiation and the microstructural analysis (see Section 4.2), the use of high dose rates and lower temperatures in the tests presented in this study would be expected to produce greater defect densities than those that may be present in the real application, thus providing a bounding case.

### 4.4 Effect of gamma energy

The gamma source employed in this work was a  $^{60}\text{Co}$  source, which has an energy spectrum with  $\gamma$  peaks at 1.1732 and 1.3325 MeV. It is possible that differences in the gamma energy spectrum between  $^{137}\text{Cs}$  (major gamma emitter in spent nuclear fuel, responsible for the highest gamma fluxes expected during the copper canister lifetime) and  $^{60}\text{Co}$  (the source used in these experiments) would induce differences in the nature of interactions between copper and the gamma rays. In particular, the characteristic energy of gamma rays emitted by  $^{60}\text{Co}$  is  $> 1$  MeV, compared with a peak energy of 0.66 MeV for  $^{137}\text{Cs}$ . These differences are such that, whilst Compton scattering (i.e. energy dispersion

through photon-electron interactions) is expected to dominate the behaviour of gamma rays emitted by  $^{137}\text{Cs}$ , generation of electron-hole pairs may be an important component of the interaction between gamma rays emitted by  $^{60}\text{Co}$  and copper. Electron-hole pair generation, however, is an energy-consuming process and its unlikely, alone, to lead to the generation of point defects. In particular, given that the energy required for the generation of an electron-hole pair is 1 MeV, the residual “kinetic” energy associated with the newly generated electrons (potentially able to generate point defects) is  $< 0.4$  MeV, which is less than the Compton energy associated with  $^{137}\text{Cs}$  gamma photons. On the other hand, for  $^{60}\text{Co}$  gamma photons that were not to generate electron-hole pairs, higher energies than those expected for  $^{137}\text{Cs}$  would be dissipated through Compton effects.

In summary, whilst the differences in energy spectra between  $^{137}\text{Cs}$  and  $^{60}\text{Co}$  may lead to differences in the way in which gamma rays interact with matter (in this case copper atoms), the fundamental mechanism of generation of point defects should be similar in both cases (generation due to interaction with electrons). The fact that the energy spectrum associated with Compton effects generated by  $^{60}\text{Co}$  bounds that of  $^{137}\text{Cs}$  suggests that the approach used in this study would have, at best, resulted in some conservatism (i.e. more defects generated) relatively to the real application.

#### 4.5 Concentration of point defects due to gamma irradiation

As discussed in Section 4.2, thermal annealing effects are likely to play a critical role in determining the concentration of point defects in a copper at room temperature, including material that was exposed to gamma radiation. In general, the steady state concentration of vacancies ( $C_v$ ) and interstitials ( $C_i$ ) in a solid under irradiation can be calculated according to the following equations (Was 2017):

$$C_v = \left[ \frac{K_0 K_{is}}{K_{iv} K_{vs}} + \frac{K_{is}^2 C_s^2}{4K_{iv}^2} \right]^{1/2} - \frac{K_{is} C_s}{2K_{iv}} \quad \text{Equation 4-1}$$

$$C_i = \left[ \frac{K_0 K_{vs}}{K_{iv} K_{is}} + \frac{K_{vs}^2 C_s^2}{4K_{iv}^2} \right]^{1/2} - \frac{K_{vs} C_s}{2K_{iv}} \quad \text{Equation 4-2}$$

where  $K_0$  is the defect production rate,  $C_s$  is the sink density, and the  $K_{xy}$  terms are rate constants for recombination (iv), interstitial loss to sinks (is) and vacancy loss to sinks (vs):

$$K_{iv} = 4\pi r_{iv} (D_i + D_v) \approx 4\pi r_{iv} D_i \quad \text{Equation 4-3}$$

$$K_{is} = 4\pi r_{is} D_i$$

$$K_{vs} = 4\pi r_{vs} D_v$$

where  $r_{xy}$  is the recombination radii (set to  $3a$  where  $a$  is the lattice parameter = 0.3 nm),  $D_i$  is the diffusion coefficient for self-interstitials in Cu and  $D_v$  is the diffusion coefficient for vacancies in Cu:

$$D_i = \alpha a^2 v \exp\left(\frac{S_m^i}{k}\right) \exp\left(\frac{-E_m^i}{kT}\right) \quad \text{Equation 4-4}$$

$$D_v = \alpha a^2 v \exp\left(\frac{S_m^v}{k}\right) \exp\left(\frac{-E_m^v}{kT}\right)$$

where  $k$  is Boltzmann’s constant ( $8.6 \times 10^{-5}$  eV  $\text{K}^{-1}$ ),  $v$  is the Debye frequency ( $10^{13}$   $\text{s}^{-1}$ ), and  $a = 1/6 zA^2$  where  $z$  is the number of nearest neighbours in the lattice and  $A$  is the nearest neighbour spacing in units of lattice parameter,  $a_0$ . For the fcc lattice interstitials,  $a = 0.5$ , and  $E_m = 0.12$  eV and for vacancies,  $a = 1.0$ , and  $E_m = 0.70$  eV. For both vacancies and interstitials the entropy term ( $S_m/k$ ) can be neglected Was (2017).

In the cases of interest here (both the tests carried out in this study and the copper canister in the real application) the rate of changes of the main environmental parameters controlling the values of the rate constants described above (i.e. the gamma flux and the temperature) are much slower than the inherent rate of the processes leading to thermal annealing. As such, the problem can be treated as a quasi-steady-state problem.

A summary of the concentration of vacancies estimated using Equations 4-1 to 4-4 in gamma irradiated copper in the experiments (5 days at room temperature at a dose rate of  $1 \text{ kGy h}^{-1}$ ) and for the real application (very long times at 50 to 90 °C at the damage rates discussed in Guinan (2001)) assuming a sink density ( $C_s$ ) of  $0.5 \times 10^{15} \text{ m}^{-2}$  (similar to the dislocation density estimated for cold worked copper in this study), is reported in Table 4-1. Table 4-1 also reports calculations for the room temperature experiment in the case of a negligible sink density, assumed to be broadly representative of well-annealed copper and providing an upper bound for the expected concentration. As a result of recombination and other annihilation processes (e.g. at grain boundaries), the concentration of both vacancies and interstitials is much less than the concentration of atoms displaced. As a result of their high diffusivity, the concentration of interstitials is orders of magnitude lower than that of vacancies and, as such, we need only consider the vacancy concentration (Was 2017). Full details of the calculations carried out are reported in Appendix B.

In the real application, assuming a high dislocation density ( $0.5 \times 10^{15} \text{ m}^{-2}$ ) and the initial damage rates in the repository calculated in Guinan (2001) ( $1.7 \times 10^{-10} \text{ dpa year}^{-1}$ , i.e.  $5.4 \times 10^{-18} \text{ dpa s}^{-1}$ ), a concentration of  $3.2 \times 10^{12} \text{ m}^{-3}$  vacancies is obtained. The vacancy concentration equates to  $3.6 \times 10^{-15} \%$  of lattice sites<sup>8</sup>. At the rate of damage expected, the steady state concentration would be reached within a few months, compared with periods of the order of hundreds of years over which gamma doses would decay. As a result of neglecting thermal annealing effects, the analysis presented in Guinan (2001) results in a substantial over-prediction of the concentration of defects since, under these assumptions, all atomic displacements result in the formation of vacancies, with a concentration of  $4 \times 10^{-9} \text{ dpa}$  ( $4 \times 10^{-7} \%$  of lattice sites).

The irradiation tests presented herein were carried out at higher dose rates and lower temperatures than that present in the real application. As such, due to both the higher damage production rate and the lower rate of annealing, steady state concentrations of defects during irradiation would be expected to be higher in the experiment than in the KBS-3 application. In calculating the concentration of vacancies in the experiment presented in this study we used the calculations presented in Guinan (2001) to focus on the  $\gamma$  energy range of interest (1.25 MeV for  $^{60}\text{Co}$ ) and scale the damage to the fluxes calculated for the experiment. With this approach we estimated displacement rates of  $3.5 \times 10^{-8} \text{ dpa year}^{-1}$  ( $1.1 \times 10^{-15} \text{ dpa s}^{-1}$ ) and resulting vacancies concentrations of  $1.3 \times 10^{17} \text{ m}^{-3}$  for a dislocation density of  $0.5 \times 10^{15} \text{ m}^{-2}$  and of  $3.9 \times 10^{18} \text{ m}^{-3}$  for a well annealed copper (the latter below steady state). It is worth noting that the damage rates estimated in these calculations are inherently self-consistent with those reported in Guinan (2001). The ratio of the gamma fluxes ( $1.2 \times 10^{14}/2.7 \times 10^{10} = 5 \times 10^3$ ) is partly compensated, in Guinan (2001), by the fact that the total damage rate computed in that case take into account not only the energies associated with  $^{60}\text{Co}$  but the whole energy spectrum associated with spent fuel, resulting in a total ratio between damage rates of  $3.5 \times 10^{-8}/1.7 \times 10^{-10} = 2 \times 10^2$ . Further details are reported in Appendix B.

After irradiation ceases (i.e. during storage and subsequent analysis), the considerations presented in Section 4.2 suggest that such defects would quickly decrease to those expected at thermal equilibrium without radiation, making it difficult to preserve any radiation-induced defect before microstructural characterisation. In fact, the concentration of vacancies decays according to  $C_v(t) = C_0/(1+K_{iv}C_0t)$  where  $C_0$  is the concentration at the termination of the experiment and  $t$  is time (see general treatment in Was 2017). For example, starting from the concentration estimated immediately after irradiation in the case of a well-annealed sample ( $3.9 \times 10^{18} \text{ m}^{-3}$ ), after one day the vacancy concentration will decay to  $2.3 \times 10^{12} \text{ m}^{-3}$ , and after 1 month, to  $7.6 \times 10^{10} \text{ m}^{-3}$ . Similarly, assuming a concentration of dislocations of  $0.5 \times 10^{15} \text{ m}^{-2}$  (representative of the copper used in these experiments), the steady

<sup>8</sup> Note that, when thermal annealing effects are neglected, the number of atoms displaced is a direct measure of the concentration of defects generated. This is not the case when thermal annealing effects are taken into account. To distinguish between the two, we report initial damage in displacements per atoms (dpa) and the concentration of resulting defects in percentage of lattice sites (%).

state concentration of vacancies would be  $1.3 \times 10^{17} \text{ m}^{-3}$ . Upon termination of the experiment, the vacancy concentration decays according to  $C_v(t) = C_0 \exp(-C_s K_v t)$  (see general treatment in Was 2017), resulting in only 10 % of vacancies remaining after 1 h and essentially none after 1 day. The much more rapid kinetics is due to the very high defect density that shortens the vacancy diffusion distance to reach a sink.

In summary, contrary to what was assumed in the simplified and conservative analysis presented in Guinan (2001), after reaching such steady state, defects would not continue to accumulate, since the generation of further defects would be compensated by their annihilation. Based on the analysis presented in this section, the concentration of point defects achievable in room temperature experiments immediately after completion of irradiation (i.e. neglecting annihilation in the period between irradiation and examination) may be of the order of  $10^{15} - 10^{17} \text{ m}^{-3}$  ( $10^{-12} - 10^{-10}$  at% of lattice sites).

**Table 4-1. Estimated quasi-steady state vacancies concentration in gamma-irradiated copper at room temperature (our tests) and at 90 °C (real application) at different assumed initial concentrations of dislocations (defect sinks). Note that the value at 90 °C has been taken directly from Guinan (2001) and not calculated as done for the values at 25 °C in this study.**

Case	T (°C)	Dose or damage rate	Initial defect density ( $\text{m}^{-2}$ )	Irradiation time	Calculated vacancy concentration
Real Application, high dislocation density (damage rate as per Guinan 2001)	90	$1.7 \times 10^{-10} \text{ dpa year}^{-1}$ (full spectrum)	$0.5 \times 10^{15}$	~100 years	$3.2 \times 10^{12} \text{ m}^{-3}$ or $3.6 \times 10^{-15}$ at% (steady state)
Experiment, high dislocation density (damage rate calculated based on Guinan 2001)	25	$1 \text{ kGy h}^{-1} {}^{60}\text{Co}$ $\sim 3.5 \times 10^{-8} \text{ dpa year}^{-1}$	$0.5 \times 10^{15}$	5 days	$1.3 \times 10^{17} \text{ m}^{-3}$ or $1.5 \times 10^{-10}$ at% (steady state)
Experiment, well-annealed sample (damage rate calculated based on Guinan 2001)	25	$1 \text{ kGy h}^{-1} {}^{60}\text{Co}$ $\sim 3.5 \times 10^{-8} \text{ dpa year}^{-1}$	0	5 days	$7.7 \times 10^{19} \text{ m}^{-3}$ or $8.6 \times 10^{-8}$ at% (steady state) $3.9 \times 10^{18} \text{ m}^{-3}$ or $4.4 \times 10^{-9}$ at% below steady state)

## 4.6 Concentration of point defects due to neutron irradiation

In the work carried out by Guinan (2001), the generation of defects as a result of neutron irradiation is calculated to be greater than the damage generated by gamma irradiation. This is because, even if generated at very low fluxes (spontaneous fission), the ability of neutrons to displace atoms and generate point defects is much greater than that of gamma photons. In particular, when neglecting thermal annealing effects, the work by Guinan (2001) suggests a total damage generated by neutrons over 100,000 years to be order of  $3 \times 10^{-7} \text{ dpa}$ , compared with the value of  $4 \times 10^{-9} \text{ dpa}$  calculated for gamma rays.

In reality, the considerations associated with thermal annealing presented in the previous sections are also going to be valid for neutrons. Although in the case of neutrons the rate of defect generation will be slightly higher than for gamma rays ( $2.4 \times 10^{-10} \text{ dpa year}^{-1}$  vs.  $1.7 \times 10^{-10} \text{ dpa year}^{-1}$  estimated in Guinan (2001), the rate of annealing will be independent on the source of damage and constrain the concentration of defects to values similar to that estimated for gamma rays. Specifically, in this case, Equation 4-1 predicts a steady-state concentration of defects of the order of  $7 \times 10^{12} \text{ m}^{-3}$  (or  $8 \times 10^{-15}$  % of lattice sites). This is much less than the concentration predicted in Guinan (2001) neglecting thermal annealing effects.

## 4.7 Sensitivity of experimental techniques

In this section we compare the sensitivity of different techniques with the concentration of defects estimated in Section 4.5 for our experimental conditions. Specifically, vacancy concentrations as low as  $10^{15}$ – $10^{17}$   $\text{m}^{-3}$  ( $10^{-12}$ – $10^{-10}$  % of lattice sites) might be expected in room temperature experiments at the dose rates and doses used in this study, reducing to thermal equilibrium concentrations over comparatively short timescales once removed from the radiation field. Due to thermal annealing effects, concentrations in the real application (90 °C) are expected to be substantially lower than those obtained in room temperature experiments, making their detection even more difficult. Based on our analysis, to detect point defects introduced by room temperature irradiation, experimental techniques deployed would need to be able to detect concentrations at least of the order of  $10^{17}$   $\text{m}^{-3}$  ( $10^{-10}$  % of lattice sites or  $10^{-3}$  ppb).

### 4.7.1 HR-TEM

A summary of the methods and capabilities of Transmission Electron Microscopy can be found in Table 4-2. High-Resolution Transmission Electron Microscopy with its variants is, in principle, capable of detection and quantification of defect structures ranging from the defects of the scale of individual atoms at high resolution (e.g. vacancy clusters) to defects in the ppb concentration range at low resolution. Specifically, assuming a lattice parameter ( $a$ ) of  $3.6 \times 10^{-10}$  m for copper and 4 atoms per unit cell, the volume occupied by a copper atom is approximately  $1.16 \times 10^{-29}$   $\text{m}^3$  (i.e.  $a^3/4$ ). Sample dimensions accessible by HR-TEM can be as low as  $0.1 \times 1 \times 1$  nm (for mono or double layers) and can be extended up to approximately  $10 \times 100 \times 100$  nm. This covers atom numbers from 9 to  $9 \times 10^6$  (i.e. provided that the resolution was sufficient, defect densities of one every ten atoms to a ppm range<sup>9</sup>).

For conventional TEM the sample volume can be expected to be in the  $20 \times 200 \times 200$  nm range up to 100 nm thickness in a  $10 \times 10$  micron area. The number of examined atoms here rises to  $10^7$  to  $10^{11}$  (i.e. provided that the resolution was sufficient, defect densities as low as  $10^{-2}$  ppb).

However, in the case of point defects (the primary species of concern in this study), a number of factors may influence the detectability of defects in TEM:

- The contrast of individual vacancies compared to the contrast caused by other mechanisms (bending contours, thickness contrast and diffraction contrast caused by other defects).
- Annihilation of point defects (e.g. vacancies and interstitials) either at the surface (most of the atoms in a TEM sample are less than 50 nm away from the surface) or at other defects, e.g. dislocations, other vacancies, and grain boundaries.

A more thorough treatment of these issues has been carried out by Daulton et al. (2000).

In principle, if we assume defect densities caused by gamma irradiation in copper of the order of  $10^{15}$ – $10^{17}$  displacements  $\text{m}^{-3}$  at room temperature and the dose rates and doses of interest (see Section 4.5), conventional TEM may get close to examine a high enough number of atoms to be able to detect these defects (if they could be somewhat resolved at their scale), whilst HR-TEM methods could be used to identify the nature of the defects. However, it appears difficult to be able to simultaneously obtain the benefits of both these techniques with the defect size and densities expected (i.e. too small, too few defects). As such, the ability of TEM to study point defects induced by gamma radiation at the concentrations of interest seems limited.

<sup>9</sup> The copper atom volume estimated above ( $\sim 10^{-29}$   $\text{m}^3$ ) results in a density of  $10^{29}$  atom  $\text{m}^{-3}$ . With a volume of  $0.1 \times 1 \times 1$  nm ( $0.1 \text{ nm}^3 = 10^{-28}$   $\text{m}^3$ ), one would be able to observe  $10^{29}$  atom  $\text{m}^{-3} \times 10^{-28}$   $\text{m}^3 = 10$  atoms. With a volume of  $10 \times 100 \times 100$  nm, about  $10^7$  atoms.

**Table 4-2. TEM capabilities and sensitivities.**

	<b>HR-TEM</b> (High Resolution Transmission Electron Microscopy) <b>HR-STEM</b> (High Resolution Scanning Transmission Electron Microscopy) <b>HAADF</b> (High Angle Annular Dark Field) <b>Identification of individual defects</b>	<b>Conventional TEM</b> In BF/DF (Bright Field/Dark Field) mode  <b>Quantification of defect numbers due to strain fields</b>
Point defects ( <b>vacancies</b> , interstitials, substitutes with atoms of different Z-number)	Difficult and potentially requires image simulation/ aberration corrected microscope Resolution theoretically < 1 Å Number of observed atoms: < 10 to low hundreds	Only possible in certain orientations, hence may need preparation of more than one sample, Low contrast for some defects and overlap with thickness and bending contrast Quantification depends on successful automation of image processing.
Small dislocation loops, Stacking faults, dislocations, and dislocation arrays	Potentially time consuming Resolution 0.1–10 nm Number of atoms observed: hundreds to (ten) thousands	Resolution: 1 nm to low micrometre range Observed number of atoms: 10 000 to several millions

#### 4.7.2 PALS

Positron annihilation is sensitive to defects in the concentration range  $10^{21}$ – $10^{26}$  m<sup>-3</sup> (Tuomisto and Makkonen 2013). For a material like Cu (lattice parameter  $\sim 3 \times 10^{-10}$  m), 1 ppm is of the order of  $10^{23}$  m<sup>-3</sup>, and this is typically what is quoted<sup>10</sup> for the experimental sensitivity of PALS. At the extreme of this range, a defect concentration of 1 in  $10^8$  atoms (10 ppb) would correspond to about a defect's concentration of  $10^{21}$  m<sup>-3</sup>, which is getting quite close to the sensitivity of the technique. In principle, as discussed above, on well annealed samples during room temperature irradiation, vacancy concentrations of the order of  $10^{-3}$  ppb might be achieved during irradiation, making the use of PALS unsuitable to detect resulting defect concentrations. On the other hand, the positrons are typically able to probe  $10^{20}$  atoms (see Section 2.3) ensuring that, at the defect concentrations estimated, a sufficiently large volume of atoms is probed to potentially detect such defects.

#### 4.7.3 Nanoindentation measurements

In principle, nanoindentation measurements could be used qualitatively to corroborate the results of the other measurements carried out in this study by measuring any changes in mechanical properties that may be induced by irradiation. However, the technique per se is less sensitive to point defects than to other type of defects (e.g. dislocations). As such, its application for this type of problem is not straightforward. As a minimum, to attempt to detect any changes in the concentration of point defects, working with control samples with greater grain size and much lower concentration of initial defects would be highly desirable. Working with greater grain size, however, would require a sufficiently large set of repeats to discount any measurements bias associated with probing different grain orientations between irradiated and control samples.

#### 4.7.4 Electrical resistivity

In the measurements carried out in this study, the difference between the resistivity measured in irradiated and unirradiated samples is substantially smaller than the uncertainty evaluated theoretically. As such, on the basis of the work carried out to date, electrical measurements indicate no meaningful difference between the irradiated and the unirradiated samples.

It may be possible to improve the sensitivity of the measurement technique deployed. This could be done by reducing the uncertainties associated with the most significant contributors (see Table 3-3), which is likely to require deploying and characterising more sensitive equipment. Improved

<sup>10</sup> A lattice parameter of  $3 \times 10^{-10}$  m is consistent with an atom volume of the order of  $0.01$  nm<sup>3</sup> or  $10^{-23}$  cm<sup>3</sup> ( $10^{-2} \times 10^{-21}$  cm<sup>3</sup>). A defect concentration of 1 ppm ( $10^{-6}$ ) is equivalent, on a volumetric scale, to 1 defect every  $10^{-17}$  cm<sup>3</sup> (i.e.  $10^{17}$  defects per cm<sup>3</sup>).



uncertainty will give more confidence in any difference/similarity between the two types of samples. However, before doing so, it is desirable to consider, theoretically, what level of sensitivity electrical measurements would require to attempt to detect point defects in the concentrations expected.

To consider this question, it is informative to consider existing theoretical frameworks linking resistivity measurements with defect concentrations. Since the electrical resistivity is proportional to the total concentration of point defects, in irradiated materials the resistivity increase per unit irradiation dose is a measure of the concentration of stable defects produced at a given irradiation temperature and dose rate. Numerous studies have been conducted that link resistivity change to defect concentration and have shown that the change in resistivity,  $\Delta\rho$ , falls in the range  $\Delta\rho \approx 1.3\text{--}3.0 \mu\Omega \text{ cm}$  per atomic percent of vacancies (Ehrhart et al. 1986, Simmons and Balluffi 1958, 1963, Meechan and Brinkman 1956, Ehrhart and Schlagheck 1974, Haubold and Martinson 1978, King and Benedek 1981)<sup>11</sup>, or:

$$\Delta\rho = (2.3 \pm 0.2) \times 10^{-6} [\Omega\text{cm}/\%] \quad \text{Equation 4-5}$$

Given that the change in resistivity per percent of vacant lattice sites is approximately  $2 \mu\Omega \text{ cm}$ , the resistivity change for the case of room temperature well-annealed samples (defect concentration  $\sim 10^{-10} \%$  see Section 4.5) would be of the order of  $10^{-4} \text{ p}\Omega \text{ cm}$ . Hence, the sensitivity of the resistivity measurement would need to be better than  $\sim 10^{-5} \text{ p}\Omega \text{ cm}$ . The relative uncertainty estimate applied to the measured resistivity value evaluated in Section 3.4 is equivalent to an uncertainty of  $50 \text{ p}\Omega \text{ m}$  (i.e.  $0.3 \%$  of  $17 \text{ n}\Omega \text{ m}$ ). On the other hand, literature studies focusing on the use of resistivity measurements for the study of point defects indicate that uncertainty on resistivity measures as low as  $5 \times 10^{-13} \Omega \text{ cm}$  ( $0.5 \text{ p}\Omega \text{ cm}$ ) could be achieved (Corbett et al. 1959), compared with changes in resistivity associated with levels of damage predicted in our analysis of the order of  $10^{-4} \text{ p}\Omega \text{ cm}$ .

## 4.8 Changes in mechanical properties

No obvious detectable difference in mechanical properties was measured through nano-indentation between irradiated and non-irradiated samples. The analysis carried out so far indicates that changes in the concentration of point defects are likely to be difficult to detect given the very low concentrations expected to result by gamma radiation (especially in samples with a high concentration of initial defects). However, the fact that nanoindentation did not detect any changes in mechanical properties provides a direct measure of the fact that whatever changes might be introduced by radiation (if any) was unable to affect hardness and modulus of the material.

---

<sup>11</sup> In general in these experiments, one measures the resistivity of the sample before irradiation, and again after irradiation to calculate the change in resistivity. Which relates it to the defect concentration as per empirical Equation 4-5. There will be a starting concentration of defects as well, but it is safe to assume that these concentrations are vanishingly small, meaning they essentially fall below the measurement capability of the instrumentation.



## 5 Conclusions

Copper samples were irradiated, under an inert atmosphere, up to a full repository dose of 100 kGy. Dose rates were approximately 1 kGy/hour, ensuring that the full dose was reached within less than a week of irradiation. Post-irradiation examination was performed on irradiated samples using High-Resolution Transmission Electron Microscopy (HR-TEM), nanoindentation, Positron Annihilation Lifetime Spectroscopy (PALS) and electrical resistivity measurements. Data from these measurements was compared against measurements done on unirradiated control samples to estimate the effect gamma irradiation had on defect density, material microstructure and selected material properties. Gamma radiation was found to have no effects on the copper's properties and microstructure within the sensitivity and "representativeness" (i.e. ability to probe volumes that produce statistically significant results) of the techniques employed. In particular:

- HR-TEM showed no detectable difference between irradiated and unirradiated samples. However, it also indicated a high concentration of dislocations, dislocation loops and stacking faults in both irradiated and control samples, which would have made it more difficult to detect any differences if these were present. A theoretical analysis of the merits of this technique indicates that, although at high magnification it is potentially sufficiently sensitive to detect point defects, confidence in the analysis (i.e. high representativeness) would require low magnification, making detection of defects in the expected concentrations difficult.
- Positron annihilation measurements indicate that there is no detectable change in the population or nature of defects after gamma irradiation. However, like HR-TEM, it also indicated a high concentration of dislocations in both samples, which would have made it more difficult to detect any differences if these were present. A theoretical analysis of the merits of this technique indicates that, although it has high "representativeness" (large volume of material probed), the sensitivity required to measure a level of damage commensurate to that expected in the copper containers on the basis of current theoretical predictions is beyond the current capabilities of the technique.
- Electrical resistivity measurements showed no detectable change between the irradiated and the unirradiated samples. A theoretical analysis of the merit of these measurements indicates that it is unlikely to have sufficient sensitivity to detect changes at the concentrations expected.
- Nanoindentation showed no detectable difference in hardness and modulus between irradiated and unirradiated samples. Correlating the results of these measurements with defect types and at the concentrations expected is likely to be even more difficult than other techniques and would require use of samples with lower initial defect density as well as larger grain size. On the other hand, the lack of changes observed with this technique provides a direct indication that "static" mechanical properties were not affected by the irradiation.

A theoretical analysis of the point defect densities expected to be generated by gamma irradiation in this experiment (25 °C) and the real application (< 95 °C) indicates that, due to thermal annealing effects, the likely maximum defect concentrations are much below the capability of current state-of-the-art techniques, making the task of measuring the concentration of such defects beyond reach. Further work could consider the use of well-annealed samples and whether the use of even higher dose rates and cryogenic temperatures during and after irradiation would make the detection of such defect concentrations possible.



## References

SKB's (Svensk Kärnbränslehantering AB) publications can be found at [www.skb.com/publications](http://www.skb.com/publications).

- Campillo Robles J M, Ogando E, Plazaola F, 2007.** Positron lifetime calculation for the elements of the periodic table. *Journal of Physics: Condensed Matter* 19, 176222. doi:10.1088/0953-8984/19/17/176222
- Čížek J, Procházka I, Vostrý P, Chmelík F, Islamgaliev R K, 1999.** Positron lifetime spectroscopy of nanocrystalline copper. 95, 487–495.
- Čížek J, Procházka I, Cieslar M, Kužel R, Kuriplach J, Chmelík F, Stulíková I, Bečvář F, Melikhova O, Islamgaliev R K, 2002.** Thermal stability of ultrafine grained copper. *Physical Review B* 65. doi:10.1103/PhysRevB.65.094106
- Corbett J W, Smith R B, Walker R M, 1959.** Recovery of electron-irradiated copper – I. Close pair recovery. *Physic Review* 114, 1452–1459.
- Daulton T L, Kirk M A, Rehn L E, 2000.** *In-situ* transmission electron microscopy study of ion-irradiated copper: temperature dependence of defect yield and cascade collapse. *Philosophical Magazine A* 80, 809–842.
- Ehrhart P, Schlagheck U, 1974.** Investigation of Frenkel defects in electron irradiated copper by Huang scattering of X-rays. I. Results for single interstitials. *Journal of Physics F: Metal Physics* 4, 1575. doi:10.1088/0305-4608/4/10/006
- Ehrhart P, Robrock K H, Schober H R, 1986.** Basic defects in metals. In Johnson R A, Orlov A N (eds). Amsterdam: Elsevier, 3–115.
- Giebel D, Kansy J, 2001.** A new version of LT program for positron lifetime spectra analysis. *Materials Science Forum* 666, 138–141.
- Guinan M W, 2001.** Radiation effects in spent nuclear fuel canisters. SKB TR-01-32, Svensk Kärnbränslehantering AB.
- Haubold H-G, Martinson D, 1978.** Structure determination of self-interstitials and investigation of vacancy clustering in copper by diffuse X-ray scattering. *Journal of Nuclear Materials* 69–70, 644–649.
- ISO, 2008.** ISO/IEC GUIDE 98-3:2008: Uncertainty of measurement – Part 3: Guide to the expression of uncertainty in measurement (GUM:1995). Geneva: International Organization for Standardization.
- King W E, Benedek R, 1981.** Computer-simulation study of the displacement threshold-energy surface in Cu. *Physical Review B* 23, 6335–6339.
- Meechan C J, Brinkman J A, 1956.** Electrical resistivity study of lattice defects introduced in copper by 1.25-MeV electron irradiation at 80 °K. *Physical Review* 103, 1193–1202.
- Oliver G M, Pharr W C, 1992.** An improved technique for determining hardness and elastic modulus using load and displacement sensing indentation experiments. *Journal of Materials Research* 7, 1564–1583.
- Sandström R, Wu R, 2013.** Influence of phosphorus on the creep ductility of copper. *Journal of Nuclear Materials* 441, 364–371.
- Schilling W, Ehrhart P, Sonnenberg K, 1975.** Interpretation of defect reactions in irradiated metals by the one interstitial model. In
- Simmons R O, Balluffi R W, 1958.** X-ray study of deuteron-irradiated copper near 10 °K. *Physical Review* 109, 1142–1152.
- Simmons R O, Balluffi R W, 1963.** Measurement of equilibrium concentrations of vacancies in copper. *Physical Review* 129, 1533–1544.

**Tuomisto F, Makkonen I, 2013.** Defect identification in semiconductors with positron annihilation: Experiment and theory. *Reviews of Modern Physics* 85, 1583–1631.

**UKAS, 2007.** M3003: The expression of uncertainty and confidence in measurement. Feltham: United Kingdom Accreditation Service.

**Was G S, 2017.** Fundamentals of radiation materials science: metals and alloys. New York: Springer.

**Zhou K, Zhang T, Wang Z, 2015.** Positron lifetime calculation for possible defects in nanocrystalline copper. *Physica Scripta* 90, 105701.

## Radiation Certificate



**Svensk Kärnbränslehantering AB (SKB)**

**Assessment of microstructural  
changes in copper due to gamma  
radiation.**

Project: WBS 208322

5<sup>th</sup> November 2018

Wood Reference: HIF 129

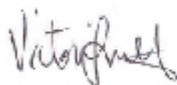
### Radiation Test Certificate

Following the recent irradiation of your pure copper samples, I provide details of the irradiation conditions and dose to which each of the samples were exposed:

<b>Irradiation Facility:</b>	Cobalt-60 Cell 5, Harwell
<b>Irradiation Type:</b>	1.25 MeV Gamma
<b>Date:</b>	30 <sup>th</sup> August – 4 <sup>th</sup> September 2018
<b>Temperature:</b>	22 ± 2°C
<b>Average Dose rate:</b>	955 Gy hr <sup>-1</sup> ±10%
<b>Total Dose:</b>	109 kGy ±10%

The dose rate measurements were made using instrumentation calibrated to national standards.

Yours Sincerely,



**Victoria Smith**  
Wood

**Correspondence:**  
Building 150  
Harwell Campus, Didcot,  
Oxfordshire, OX11 0QB  
United Kingdom  
Tel +44 (0)1635 280384  
Fax +44 (0)1635 280301

**Registered office:**  
Booths Park  
Chelford Road, Knutsford,  
Cheshire, WA16 8QZ  
United Kingdom  
Registered in England  
No. 1675285





### Damage Calculations

In this section we calculate the concentrations of vacancies and interstitials for a range of cases of interest based on the equations presented in Section 4.5. We do so by first identifying or calculating damage rates ( $K_0$ ) and then by computing resulting defect concentrations at two temperatures and initial dislocation densities. For the experiment presented in this document, we estimate damage rates based on the analysis presented in (Guinan 2001).

#### Damage rate calculated in the real application

In this case, the damage (for both gammas and neutrons) is calculated based on the damage rates estimated in (Guinan 2001) for the whole energy spectrum. These are  $1.7 \times 10^{-10}$  dpa year<sup>-1</sup> ( $5.4 \times 10^{-8}$  dpa s<sup>-1</sup>) for gamma and  $2.4 \times 10^{-10}$  dpa year<sup>-1</sup> ( $7.6 \times 10^{-18}$  dpa s<sup>-1</sup>) for neutrons.

#### Damage rate calculated scaling the calculations in (Guinan 2001) to experimental fluxes

The calculations described in (Guinan 2001) reports a damage rate of  $1.7 \times 10^{-10}$  dpa year<sup>-1</sup> for a gamma energy of  $4.4 \times 10^{-16}$  eV s<sup>-1</sup> (page 19, position I), i.e. a proportionality factor between energy and damage rate ( $\kappa$ ) of  $3.9 \times 10^5$  dpa year<sup>-1</sup>/eV s<sup>-1</sup> ( $1.7 \times 10^{-10}$  dpa year<sup>-1</sup>/ $4.4 \times 10^{-16}$  eV s<sup>-1</sup>).

The calculations in Table 3 of (Guinan 2001) also indicate that, for the  $\gamma$  energy peak associated with <sup>60</sup>Co (1.25 MeV), a flux ( $\phi$ ) of  $2.7 \times 10^{-10}$  m<sup>-2</sup> s<sup>-1</sup> and an eV cross section ( $\sigma_{DE}$ ) of  $7.6 \times 10^{-3}$  barn keV were calculated. The damage rate due to the <sup>60</sup>Co component of the spectrum calculated with these values ( $K_0 = \sigma_{DE} \phi \kappa$ ) is  $7.9 \times 10^{-12}$  dpa year<sup>-1</sup>, which is about 1/100<sup>th</sup> of the total damage rate associated with the full energy spectrum ( $1.7 \times 10^{-10}$  dpa year<sup>-1</sup>). By multiplying the ratios of gamma fluxes between the experiment and the real application for the damage rates estimated above we obtain:  $K_{0,exp} = (\phi_{exp}/\phi_{app})(K_{0,app}) = (1.2 \times 10^{14}/2.7 \times 10^{10}) \times (7.9 \times 10^{-12})$  dpa year<sup>-1</sup> =  $3.5 \times 10^{-8}$  dpa year<sup>-1</sup> ( $1.1 \times 10^{-15}$  dpa s<sup>-1</sup>).

#### Concentrations of vacancies and interstitials

Before calculating concentrations of vacancies we calculate diffusivity values at relevant temperatures (293K and 363K) using the values of the input parameters described in Section 4.5. This yields diffusivity values of the order of  $10^{-16}$ – $10^{-18}$  m<sup>2</sup> s<sup>-1</sup> for vacancies and of  $10^{-9}$  m<sup>2</sup> s<sup>-1</sup> for interstitials. It is also necessary to convert estimated dislocation densities (m<sup>-2</sup>) into a sink density (m<sup>-3</sup>). This can be done by treating the dislocation line as discrete sinks and using a suitable capture radius (assumed  $3a_0$  in our calculations) to break up the line into discrete sinks. This basically transforms a solid line into discrete sinks with spacing  $3a_0$ .

Given the diffusivities and damage rates calculated above and in the previous sections, we then calculate steady-state concentrations of vacancies and interstitials implementing Equations 4-1 to 4-3 described in Section 4.5. The results of such calculations are implemented in a spreadsheet and reproduced below. As a result of their much higher diffusivity the concentration of interstitials is much less than that calculated for vacancies. The resulting steady-state concentration of vacancies has been reproduced in Table 4-1 in Section 4.5 (gammas) and in Section 4.6 (neutrons).

For one calculation (room temperature experiment with well-annealed samples) irradiation times are much less than the timescales required to reach steady state and concentrations at the times of interest have also been calculated using the equation presented in Section 4.5.

## INPUT

Case	Temperature T (°C)	Displacement rate K0 (dpa/s)	Displacement rate K0 (dpa/y)	Vacancy migration energy Emv (eV)	Interstitial migration energy Emi (eV)	lattice parameter a <sub>0</sub> (nm)	recombination radius (a <sub>0</sub> )	sink density (m <sup>-2</sup> )
γ real application (90 °C), cold worked based on (Guinan 2001)	90	$3.50 \times 10^{-18}$	$1.70 \times 10^{-10}$	0.7	0.12	0.3	3	$5.00 \times 10^{14}$
γ experiment (25 °C), cold worked based on (Guinan 2001)	25	$1.10 \times 10^{-15}$	$3.47 \times 10^{-8}$	0.7	0.12	0.3	3	$5.00 \times 10^{14}$
γ experiment (25 °C), annealed based on (Guinan 2001)	25	$1.10 \times 10^{-15}$	$3.47 \times 10^{-8}$	0.7	0.12	0.3	3	$5.00 \times 10^9$
In real application (90 °C), cold worked based on (Guinan 2001)	90	$7.64 \times 10^{-18}$	$2.41 \times 10^{-10}$	0.7	0.12	0.3	3	$5.00 \times 10^{14}$

## CALCULATED INTERMEDIATE PARAMETERS

	Atom volume omega (m <sup>3</sup> )	Vacancy diffusion coefficient Dv (m <sup>2</sup> /s)	Interstitial diffusion coefficient Di(m <sup>2</sup> /s)	Rate constant for recombination Kiv(m <sup>3</sup> /s)	Rate constant for interstitials going to sinks Kis(m <sup>3</sup> /s)	Rate constant for vacancies going to sinks Kvs(m <sup>3</sup> /s)	Sink density Cs(m <sup>-3</sup> )	Displacement rate Rd(m <sup>-3</sup> s <sup>-1</sup> )
γ real application (90 °C), cold worked based on (Guinan 2001)	$6.75 \times 10^{-30}$	$1.72 \times 10^{-16}$	$9.71 \times 10^{-9}$	$1.10 \times 10^{-16}$	$1.10 \times 10^{-16}$	$1.94 \times 10^{-24}$	$4.42 \times 10^{22}$	$2.80 \times 10^{11}$
γ experiment (25 °C), cold worked based on (Guinan 2001)	$6.75 \times 10^{-30}$	$1.30 \times 10^{-18}$	$4.20 \times 10^{-9}$	$4.75 \times 10^{-17}$	$4.75 \times 10^{-17}$	$1.48 \times 10^{-26}$	$4.42 \times 10^{22}$	$8.80 \times 10^{13}$
γ experiment (25 °C), annealed based on (Guinan 2001)	$6.75 \times 10^{-30}$	$1.30 \times 10^{-18}$	$4.20 \times 10^{-9}$	$4.75 \times 10^{-17}$	$4.75 \times 10^{-17}$	$1.48 \times 10^{-26}$	$4.42 \times 10^{17}$	$8.80 \times 10^{13}$
In real application (90 °C), cold worked based on (Guinan 2001)	$6.75 \times 10^{-30}$	$1.72 \times 10^{-16}$	$9.71 \times 10^{-9}$	$1.10 \times 10^{-16}$	$1.10 \times 10^{-16}$	$1.94 \times 10^{-24}$	$4.42 \times 10^{22}$	$6.10 \times 10^{11}$

## OUTPUT

Case	Steady state vacancy concentration Cvss (m <sup>-3</sup> )	Steady state interstitial concentration Ciss (m <sup>-3</sup> )	Steady state vacancy concentration percentage Cvss (at %)	Rate constant for onset of vacancy loss to sinks t3 (s)	Rate constant for onset of mutual recombination t1 (s)	Rate constant for onset of interstitial loss to sinks t2 (s)	Cv for expt calculated from "RT annealing..." sheet (m <sup>-3</sup> )	Cv for expt calculated from "RT annealing..." sheet (%)
γ real application (90 °C), cold worked based on (Guinan 2001)	$3.26 \times 10^{12}$	$5.77 \times 10^4$	$3.62 \times 10^{-15}$	$1.16 \times 10$	$1.80 \times 10^2$	$2.06 \times 10^{-7}$		
γ experiment (25 °C), cold worked based on (Guinan 2001)	$1.35 \times 10^{17}$	$4.19 \times 10^7$	$1.50 \times 10^{-10}$	$1.53 \times 10^3$	$1.55 \times 10$	$4.76 \times 10^{-7}$		
γ experiment (25 °C), annealed based on (Guinan 2001)	$7.70 \times 10^{19}$	$2.39 \times 10^{10}$	$8.56 \times 10^{-8}$	$1.53 \times 10^8$	$1.55 \times 10$	$4.76 \times 10^{-2}$	$3.94 \times 10^{18}$	$4.38 \times 10^{-9}$
In real application (90 °C), cold worked based on (Guinan 2001)	$7.10 \times 10^{12}$	$1.26 \times 10^5$	$7.89 \times 10^{-15}$	$1.16 \times 10$	$1.22 \times 10^2$	$2.06 \times 10^{-7}$		



